Journal of Nuclear Materials 448 (2014) 420–435

Contents lists available at ScienceDirect

Journal of Nuclear Materials

journal homepage: www.elsevier.com/locate/jnucmat

Advanced oxidation-resistant iron-based alloys for LWR fuel cladding ☆

K.A. Terrani [a,*], S.J. Zinkle [b], L.L. Snead [c]

[a] Fusion and Materials for Nuclear Systems Division, Oak Ridge National Laboratory, Oak Ridge, TN 37831, USA
[b] Nuclear Science and Engineering Directorate, Oak Ridge National Laboratory, Oak Ridge, TN 37831, USA
[c] Materials Science and Technology Division, Oak Ridge National Laboratory, Oak Ridge, TN 37831, USA

ARTICLE INFO

Article history:
Available online 1 July 2013

ABSTRACT

Application of advanced oxidation-resistant iron alloys as light water reactor fuel cladding is proposed. The motivations are based on specific limitations associated with zirconium alloys, currently used as fuel cladding, under design-basis and beyond-design-basis accident scenarios. Using a simplified methodology, gains in safety margins under severe accidents upon transition to advanced oxidation-resistant iron alloys as fuel cladding are showcased. Oxidation behavior, mechanical properties, and irradiation effects of advanced iron alloys are briefly reviewed and compared to zirconium alloys as well as historic austenitic stainless steel cladding materials. Neutronic characteristics of iron-alloy-clad fuel bundles are determined and fed into a simple economic model to estimate the impact on nuclear electricity production cost. Prior experience with steel cladding is combined with the current understanding of the mechanical properties and irradiation behavior of advanced iron alloys to identify a combination of cladding thickness reduction and fuel enrichment increase (~0.5%) as an efficient route to offset any penalties in cycle length, due to higher neutron absorption in the iron alloy cladding, with modest impact on the economics.

1. Introduction

In 1975 Hyman Rickover summarized the key considerations that led to his decision almost three decades earlier to use zirconium alloys for the fuel cladding in U.S. Navy's pressurized water nuclear reactor [1].

Almost four decades later, zirconium alloys enjoy a monopoly for uranium oxide fuel cladding material in light water reactors (LWRs) and are used in other fuel bundle structures such as portions of the grid spacers, as the channel box material for boiling water reactor (BWR) fuel assemblies, and elsewhere. Zirconium triumphed over other fielded clad options such as stainless steel, beryllium, and aluminum due to a combination of its small neutron capture cross section, reasonable corrosion resistance, and structural integrity under envisioned operating conditions. Today, zirconium alloy technology benefits from decades of active research and development, enabling tailored alloy chemistries and production techniques for optimized performance under pressurized or boiling water reactor conditions. The ongoing development activities have led to the introduction of new generations of zirconium-based alloys that exhibit enhanced corrosion resistance while limiting the detrimental irradiation effects (i.e., growth and creep) to those that are frequently inconsequential to reactor operation [2]. As summarized by Edsinger [3], these metallurgical enhancements, combined with incremental improvements in management for optimized reliability over the decades, have led to an impressive record of fuel reliability for the current zirconium-alloy cladding. To achieve this milestone, zirconium-alloy-cladded fuel production, fuel bundle handling, core operation, and water chemistry control have all been simultaneously optimized and improved over this time period.

This manuscript reexamines iron-based alloys for their potential application as nuclear fuel cladding to replace zirconium alloys. The motivation behind this effort is twofold. First, specific limitations with zirconium alloys under both design-basis and beyond-design-basis nuclear reactor accident scenarios provide incentive to explore alternative cladding options that may enable improved accident tolerance while maintaining good performance under normal operating conditions. These limitations are perceived to be serious, and therefore a renewed discussion is needed in the technical and policy communities.

Secondly, several new generations of increasingly higher performance steels are now commercially available that may offer significant performance improvements over the relatively simple austenitic steels that were utilized as cladding in some early commercial fission reactors [4]. Both alloy systems were successful in their early application, although zirconium alloys ultimately

☆ The United States Government retains, and by accepting the article for publication, the publisher acknowledges that the United States Government retains, a non-exclusive, paid-up, irrevocable, worldwide license to publish or reproduce the published form of this work, or allow others to do so, for United States Government purposes.

* Corresponding author. Tel.: +1 865 576 0264.
E-mail address: terranika@ornl.gov (K.A. Terrani).

0022-3115/$ - see front matter © 2013 Elsevier B.V. All rights reserved.
http://dx.doi.org/10.1016/j.jnucmat.2013.06.041

prevailed largely owing to their reduced thermal neutron cross section—a clear advantage over iron alloys for compact submarine reactor application. Driven by the nuclear navy, the zirconium alloy system became the focus of significant R&D, resulting in alloys with superior combined nuclear and corrosion performance and a ready-made commercial infrastructure. Finally, superior stress corrosion cracking resistance in BWRs drove the complete phase out of stainless steel claddings. However, given the significant progress over the past five decades in advanced steel making, including corrosion-resistant steels (combined with our present understanding of chemistry control and environmental effects), high-strength steels, and the ability to form thin-walled tubing, it appears clear that the commercial steels utilized in the early commercial reactors can be significantly improved upon, much as the zirconium alloys were improved upon since the days of Rickover's program.

A review of the limitations with the current zirconium alloy system under design-basis and beyond-design-basis accident scenarios is offered. This review also provides simple metrics to guide selection of new clad materials. Based on the findings of a recent experimental survey of the high-temperature steam oxidation kinetics of historic, present-day commercial, and advanced steels [5], the potential to achieve higher margins of safety through replacement of zirconium alloys with advanced iron-based alloys inside LWR cores is showcased with a simplified set of analyses. A review of earlier generation stainless steels as nuclear fuel cladding in LWRs is provided and the anticipated performance of advanced iron-based alloys is briefly evaluated from a materials and environmental performance perspective, focusing on irradiation behavior, corrosion, and mechanical integrity under LWR normal operating conditions. Finally, the reactor physics characteristics and the impact on economics of nuclear electricity production upon adoption of advanced steel nuclear fuel cladding is examined with a specific set of case studies. In this manner, impactful areas for future targeted R&D in this area are identified and a broad basis for consideration of these advanced cladding concepts is provided.

2. Limitations with zirconium alloy cladding

Given decades of active research and development, today's zirconium alloy cladding technology exhibits optimized behavior under normal operating conditions where the fuel rod failure rate (typically involving a localized breach of the cladding) is on the order of a few ppm per year. Industry-led fuel reliability programs with a long-term focus have resulted in dramatic reductions in the number of fuel failures across the LWR fleet [6]. These improvements in fuel performance are concomitant with the overall trend in the industry to push the fuel burnup and duty index[1] to higher levels [7]. The overall state of the remaining limitations of the zirconium alloy cladding under normal operating conditions (given the current power and burnup trends) is a secondary concern compared to that of accident scenarios. The focus of this section is on the latter.

2.1. Limitations under postulated design-basis accidents

If one examines the regulatory requirements defining the reactor design criteria, it quickly becomes obvious that a significant portion are associated with specific performance limitations in the zirconium alloy cladding system under accident scenarios. Starting with design-basis accidents (DBA: postulated accidents that set the design criteria), two standard scenarios can be examined: loss-of-coolant accidents (LOCAs) and reactivity insertion accidents (RIAs). In case of LOCAs, the current US regulatory language limits peak clad temperature (PCT) to 1204 °C and equivalent cladding reacted (ECR) to 17% of initial cladding thickness [8]. Both of these limits are based on experiments performed on unirradiated zirconium cladding and are specific to that alloy, being driven by the susceptibility to excessive oxygen dissolution in the remaining metal that will in turn result in a brittle material in the post-quench condition [9]. Fig. 1 shows three distinct layers across a Zircaloy-2 specimen oxidized isothermally at 1200 °C in a high-pressure steam environment for 2 h. Details of the experimental apparatus are provided elsewhere [10]. It is worth noting at high temperatures (>1100 °C) the effect of steam pressure on Zircaloy oxidation kinetics is negligible [11]. The cross section consists of an oxide layer on the surface, followed by the oxygen-stabilized α-Zr(O) layer, and the β-Zr phase in the center. The remaining β-Zr layer is the only source of ductility in this partially reacted cladding. At temperatures above 1200 °C, the increased oxygen solubility in the β-Zr phase causes reduced ductility of this layer in the post-quenched condition. Rapid oxide layer growth and increased solubility of oxygen in the β-Zr phase at temperatures above 1200 °C result in loss of ductility in the cladding and constitute the regulatory basis pertinent to a design basis LOCA.

At higher burnups, however, cladding experiences further embrittlement due to hydrogen absorption as a result of waterside corrosion of the rod and hydride-phase precipitation. Recent studies show that the hydrogen present in the cladding lowers the creep resistance and increases the extent of oxygen dissolved in the metal during the oxidation phase [12–14]. These burnup effects collectively exacerbate ductility loss in the cladding in the post-quench condition [15]. Accordingly new regulatory criteria, DG-1263, have been proposed [16], based on previous observations from in-cell tests [9], to take into account the effect of hydrogen buildup in the cladding throughout the fuel operation lifetime (Fig. 2).

In the case of RIAs, the basis for regulatory criteria dates back to the 1970s and aims to set a maximum limit on energy deposition in the fuel during the transient. The fuel failure mechanism under an RIA is a function of burnup: at low burnups (<40 MWd/kgU), post-departure from nucleate boiling (DNB) phenomena is limiting, whereas at higher burnups, pellet-cladding mechanical interaction (PCMI) is the dominant failure mechanism [17]. The

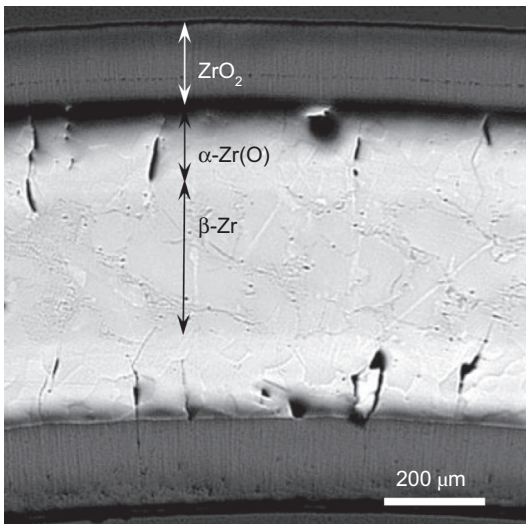

Fig. 1. Optical micrograph of the cross section of a BWR 9 × 9 bundle geometry Zircaloy-2 cladding specimen oxidized at 1200 °C for 2 h in 1 MPa steam.

[1] Fuel duty index is defined as the integral of the product of local average cladding oxide layer outer surface temperature and time: $FDI = 10^{-5}\int(T_{ave} - 580)tdt$, where the temperature is in °F and time is in *h*.

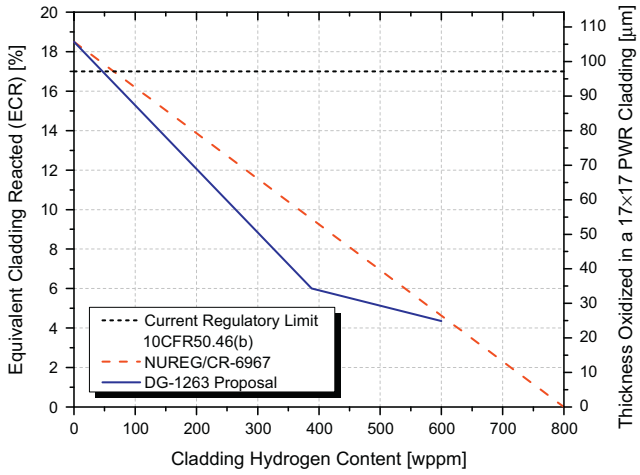

Fig. 2. Current regulatory limit on cladding oxidation [8] as well as proposed limits to take into account the effect of hydrogen [9,16].

energy deposition limits for fresh fuel rods (628 J/g of UO_2) are set based on early studies and are indeed very conservative for the low-burnup regime. As burnup increases (>40 MWd/kgU), the fuel-cladding gap disappears due to swelling of the urania pellet and cladding creepdown. As was also mentioned, hydrogen absorption in the zirconium during the fuel operation results in embrittlement of the cladding. The combination of these two effects shifts the mechanism of fuel rod failure to PCMI under RIAs. These effects have been studied extensively, and a new set of regulatory criteria have now been proposed to account for these observations for higher burnup fuel (Fig. 3) [17,18].

Note that in both cases, for design basis LOCA and RIA, hydrogen content can significantly limit cladding performance. Hydrogen is absorbed in the zirconium alloy cladding predominantly as a result of cladding oxidation by water. The atomic hydrogen that is the by-product of that reaction may diffuse into the metal to dissolve in the metal matrix (~15–20% of the amount produced). Therefore any reduction in the extent of cladding oxidation (waterside corrosion) throughout the fuel operational lifetime (~5 years) directly reduces the extent of hydrogen buildup in the fuel. Understanding this relationship has largely shaped the basis of the approach taken by fuel vendors to comply with newly proposed regulatory criteria: introduction of zirconium alloys that exhibit slower oxidation kinetics under normal operating conditions and therefore a lower hydrogen absorption rate. This trend is shown in Fig. 4, where a reduction in cladding oxide thickness as a function of burnup is apparent in the zirconium alloys developed over the past two decades (ZIRLO, M5, AXIOM alloys) compared to historic alloys such as Zircaloy-4.

2.2. Limitations under beyond-design-basis accidents

A beyond-design-basis accident (BDBA) by definition cannot be precisely defined, though it encompasses any accident scenario not considered during the definition of the design characteristics for the nuclear plant since the probability of its occurrence is deemed too low (occurrence probability of $<10^{-4}$ per reactor-year [22]). However, in the interest of continuous improvement in the safety of nuclear power plants, it is prudent to evaluate the consequences of low-probability events such as what occurred at the Three Mile Island and more recently at the Fukushima Daiichi power plants. Considering BDBA accident scenarios where the clad temperature exceeds the PCT limit of 1204 °C, the zirconium alloy cladding system proves readily susceptible to severe degradation. This is specifically the case when cooling capability inside the core becomes compromised and the cladding is exposed to high-temperature steam for prolonged periods. The thermal hydraulic heat transfer coefficient from the cladding outer diameter to the flowing water coolant under normal operating conditions is on the order of 1 W/cm^2 K [23]. The magnitude of this parameter could drop significantly, as much as four orders of magnitude, under accident conditions when the fuel is exposed to slowly flowing or stagnant steam [23–25]. Due to the poor cladding-to-steam heat conductance, decay heat drives up the fuel temperature. Once the fuel temperature reaches a sufficiently high value, zirconium undergoes rapid oxidation in the high-temperature steam environment. The exothermic zirconium-steam reaction is accompanied by an exceptionally large enthalpy of oxidation (−586 kJ/mole Zr [26]) while also resulting in rapid hydrogen production. The enthalpy production as a result of the oxidation reaction adds to the decay heat generation inside the fuel to exacerbate the rate of temperature increase in the fuel. The Arrhenius dependence of the parabolic zirconium oxidation kinetics [27] implies the heat generation due to steam oxidation of the zirconium cladding will eventually surpass the decay heat generation in magnitude. Consequently a rapid temperature excursion in the cladding is experienced that results in oxidation of the entire cladding, given that the conditions inside the core are not that of steam starvation.

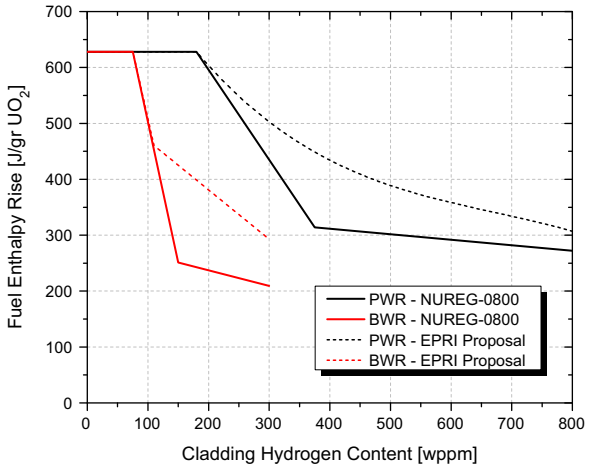

Fig. 3. Regulatory limit [18] and industry-proposed limits [17] on energy deposition into the fuel during an RIA.

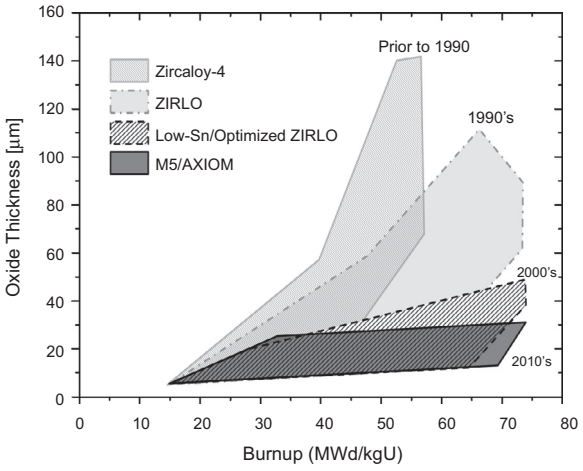

Fig. 4. Cladding oxide layer thickness as a function of burnup using literature data for conventional Zircaloy-4 and ZIRLO [19], M5 [20], and AXIOM [21] alloys.

To estimate the evolution of temperature in the fuel during an accident and to pinpoint the effect due to cladding oxidation, a simplified analysis, adopted after Olander [28], can be performed. More sophisticated analyses have been performed by Olander [29] as well as others [30,31] and detailed computer codes to simulate the entire core and auxiliary systems under accident scenarios exist [32,33]. The simplified analysis presented here is sufficient to underline inherent limitations of zirconium alloy cladding under BDBA scenarios. The high-level findings presented here are in agreement with a more detailed full core analysis [34]. The details of this methodology as well as the underlying assumptions are outlined in Appendix A. At the start of the calculation, it is assumed that the uniform temperature in the fuel and cladding is 910 and 900 °C, respectively. Cladding-to-steam heat conductance and the steam temperature are assumed to be at constant values of 1.2×10^{-3} W/cm^2 K and 900 °C, respectively, both of which are indeed simplified assumptions in this analysis. The results of the analysis are particularly sensitive to the cladding-to-steam heat conductance that spans a wide range of values and can be as high as 10^{-2} W/cm^2 K during a large break LOCA [24]. Steam temperature during accidents can vary over a broad range (few hundred degrees to well over a thousand) and increases along with the cladding temperature. A constant value of 900 °C steam temperature was assumed as an appropriate average value for the purpose of this simple analysis. The fuel geometry is assumed to be that of a rod in a 17 × 17 pressurized water reactor (PWR) bundle operating at 250 W/cm linear heat generation rate (LHR) under normal operating conditions.

Fig. 5 shows the calculated cladding temperature as a function of time after it is exposed to steam in the core. The different curves correspond to various periods of cooling after reactor scram with an active emergency core-cooling system (ECCS) before it ceases to function. In this simple analysis it is assumed that once the cooling period has ended, all cooling capability is lost inside the core and the fuel is exposed to 900 °C steam. At low temperatures (<1200 °C), the slope of the curves is governed by the value of the decay heat production term; for longer active core cooling periods, the decay heat is reduced and the rate of rise in fuel temperature upon exposure to steam (near adiabatic conditions) is smaller. However, once the cladding temperature reaches above ~1200 °C, coinciding with the NRC-specified PCT under design basis LOCA, the rate of temperature rise in the fuel rapidly increases. This rapid increase is due to the very high zirconium alloy oxidation rate above 1200 °C in steam combined with the large magnitude of the zirconium heat of oxidation. This rapid temperature rise in the cladding quickly results in complete consumption of the zirconium and release of a large amount of heat, and associated hydrogen, inside the core. In Fig. 5 the maximum cladding temperature is lower for curves with longer active cooling periods since a higher fraction of the metal undergoes oxidation at temperatures below 1200 °C. However, even after long active core cooling periods, rapid enthalpy deposition and hydrogen production in the core as a result of cladding oxidation are shown to take place within the framework of this analysis. Note that during an actual accident, extensive core degradation and relocation will be experienced before the peak cladding temperatures shown in Fig. 5 are reached. Extensive reviews of the set of physical and chemical degradation phenomenon in the complex LWR cores are given elsewhere [35,36]. Also rod-wall radiative heat transfer becomes an important means of energy dissipation at such high cladding temperatures that increases the magnitude of the overall heat transfer coefficient for the rod. In special cases, steam starvation could occur that lowers the heat generation rate due to oxidation and results in dissolution of the oxide layer on the surface of the cladding [27,29] and fuel bundle degradation and relocation [37]. These factors are not considered in the simplified analysis presented here.

It is useful to examine the two components of the LHR in the fuel rod, one due to decay heat generation and the other as a result of the oxidation reaction, as a function of time after the rod is exposed. Fig. 6 shows the evolution in these two components as a function of time along with the cladding temperature for the curve in Fig. 5 with 8 h of active cooling. While LHR due to the decay heat production (LHR_{decay}) in the fuel is undergoing a very slow decay and is largely unchanged during the time period shown in Fig. 6, the LHR as a result of cladding oxidation (LHR_{ox}) varies by many orders of magnitude after fuel is exposed. At low cladding temperatures, LHR_{ox} is orders of magnitude smaller than that of LHR_{decay}. However, at ~1200 °C, again coinciding with the NRC PCT limit, the LHR_{ox} surpasses LHR_{decay} in magnitude and continues to increase rapidly along with cladding temperature. In other words, zirconium cladding oxidation in high-temperature steam environments with poor heat transfer to the gaseous phase is characteristic of a self-catalytic process.

2.3. Limitations during used nuclear fuel disposition

One final area of importance is the susceptibility of zirconium alloy cladding materials to deteriorate during used nuclear fuel storage. Hydrogen that is present inside the cladding as a result

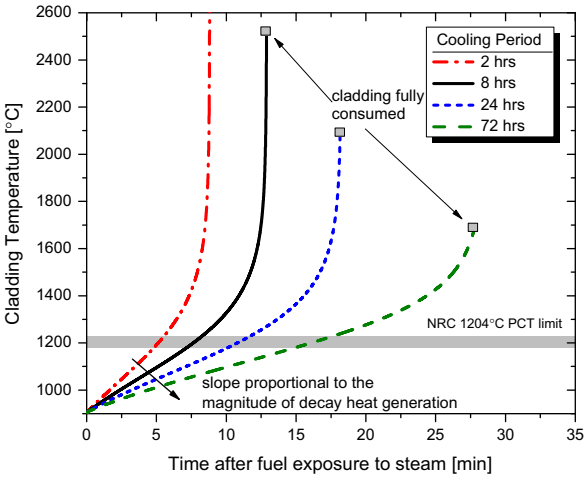

Fig. 5. Cladding temperature evolution upon exposure to 900 °C steam after various active core cooling periods.

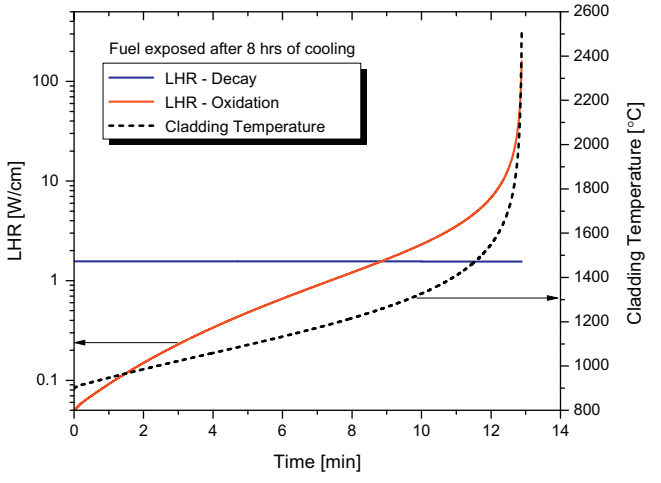

Fig. 6. Evolution of linear heat generation rate due to decay heat production and cladding oxidation along with cladding temperature as a function of time for a fuel rod exposed to 900 °C steam after 8 h of active cooling.

of fuel operation in the LWR core precipitates to form zirconium hydride platelets in the circumferential orientation. Once the fuel rods are extracted from the storage pool and prior to transfer into the dry cask storage units, they undergo a drying process to remove any water from the assemblies. Given the specifics of the drying process, the temperatures can range between 250 and 400 °C. At higher temperatures, hydride dissolution takes place due to the increased solubility of hydrogen in the metal matrix. Upon cooling the hydrides will re-precipitate. However, the presence of large azimuthal stresses in the fuel due to the rod internal pressure favors a radial orientation for these newly formed hydrides if the hoop stress is >75 MPa during cooling from 400 °C [38]. The radial hydrides greatly increase the susceptibility of the cladding to failure under stress that can result in the release of fission products into the cask. Localized corrosion of the failed fuel rods due to the presence of any leftover moisture also poses a threat to the integrity of the spent fuel bundles.

3. Gains in safety margins using advanced oxidation-resistant iron-based alloys

In order to reduce the slope of the rapid temperature excursions in the cladding and thereby gain valuable additional coping time during severe accidents, the magnitude of LHR_{ox} needs to be suppressed. One way to achieve this is to consider materials that exhibit slower steam oxidation kinetics than zirconium alloys.

A recent set of experiments was undertaken to examine high-temperature 1–20 bar steam oxidation behavior of a wide variety of iron-based alloys and SiC-based materials with the results benchmarked against standard zirconium alloys [5,10,39,40]. A number of alloys exhibited promise and will undergo further BDBA-relevant testing, and associated analysis. For this paper, two alloy classes will be highlighted for discussion. The first alloy, Kanthal APMT, is a ferritic alloy with the nominal composition of Fe–22 wt.%Cr–5Al–3Mo. This alloy is one example of a class of alumina-forming ferritic alloys that includes a wide range of Cr and Al and oxide dispersion strengthened (ODS) variants with increased creep resistance at high temperature. The other alloy selected for discussion is a standard commercial austenitic 310 stainless steel: Fe–25Cr–20Ni–2Mn. These alloys generically represent the two major types of high-temperature oxidation resistant alloys distinguished by the type of protective surface oxide or scale formed via selective oxidation: Al_2O_3 on APMT and Cr_2O_3 on 310SS.

High temperature oxidation protection, especially in steam, is more readily and robustly accomplished by selective oxidation of one bulk component of the alloy (Al or Cr) than via coatings. Moreover, a strategy where oxidation resistance is inherent to the alloy offers complete surface (internal and external) protection against steam attack and would avoid any spalling or corrosion issues during service as well as cladding burst during accident conditions, which may be problematic with coatings or composite structures. A recent investigation of composite Zr-steel concepts showed high temperature interdiffusion of Fe, Cr and especially Ni to be a significant issue [41].

Fig. 7 provides a comparison between the parabolic rate constant in steam oxidation (k_p) for zirconium alloys [26,27,42–45], the historical 304 austenitic stainless steel [46,47], and recent data for APMT and 310SS [5]. The details of the oxidation mechanism for zirconium alloys at elevated temperatures have been studied at great length and are available in the cited references. In short, the reaction kinetics are limited by oxygen diffusion through the growing oxide layers (ZrO_2 and α-Zr(O)) thus resulting in the observed parabolic behavior. For alumina-forming Fe-base alloys, once a protective α-Al_2O_3 scale has formed, generally at temperatures above 800 °C, the reaction is also limited by diffusion across this layer, likely by the transport of OH^- ions in steam [48].

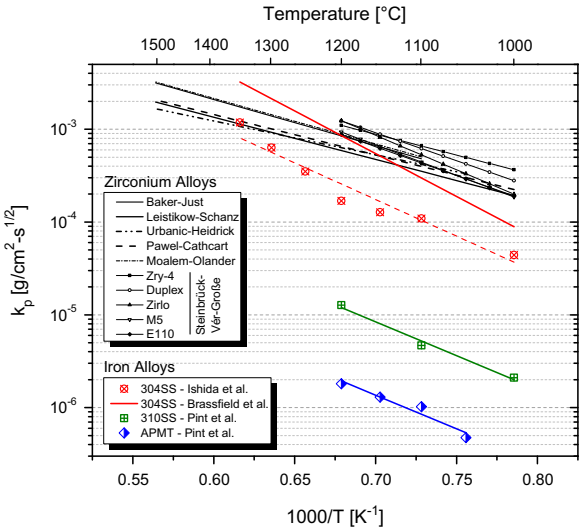

Fig. 7. Arrhenius plot of the parabolic weight-gain rate constants for zirconium alloys and 304SS oxidized in pure steam. Results from 310SS and APMT oxidation in Ar–50%H_2O environment (Ar used as carrier gas) are also shown for comparison. All tests were performed at atmospheric pressure.

In addition to the slower oxide growth kinetics shown in Fig. 7, alumina-forming Fe-base alloys have an advantage in the presence of H_2O due to the higher stability of Al_2O_3 compared to Cr_2O_3 [49]. Austenitic steels such as 304SS and 310SS can experience accelerated Cr loss and oxidation rates due to the formation of a volatile oxy-hydroxide, $CrO_2(OH)_2$ which has linear kinetics. However, in steam oxidation, little free O_2 is present to form any oxy-hydroxide and the accident time frame is too short for the associated para-linear reaction kinetics [50,51] to be of concern. Screening of various chromia-forming ferritic and austenitic steels found that Cr contents higher than 20% were needed for protective behavior in steam at 1200 °C [5]. As will be discussed in a latter section this would limit irradiation performance of these alloys.

Examination of Fig. 7 offers multiple insights that are essential for the discussion presented here. First, the oxidation rates of various zirconium alloys (historic as well as recent alloys) in high-temperature steam are very similar at temperatures >1050 °C, above the region of susceptibility (~800–1000 °C) to breakaway oxidation [9,45]. The various alloying elements in zirconium alloys that play an important role during high-temperature water corrosion (300–500 °C) show little or no effect on oxidation at high temperature. Although the historic 304SS steel cladding contains ~18% Cr, this alloy is unable to form a protective Cr-rich oxide in steam at these temperatures, like 310SS with 25%Cr and 20%Ni. Thus, the kinetics reflect the rapid formation of FeO_x with oxidation rates on the same order as that of zirconium alloys. On the other hand, the magnitude of the parabolic oxidation rate constants for APMT and 310SS, are roughly two to three orders of magnitude lower than what is observed for zirconium alloys.

A simplified calculation, given the framework discussed in Appendix A, can now be performed to illustrate gains in safety margins if a transition away from zirconium alloy cladding and toward more oxidation-resistant materials is made. Fig. 8 shows the evolution in fuel temperature once it becomes exposed to steam for various magnitudes of oxidation rate. For this calculation the Arrhenius dependence of the oxidation rate is conserved at what is reported for zirconium alloys (84 kJ/mole Zr [42]) and only the rate constant has been fractionally reduced in this parametric study. Also the enthalpy of oxidation that governs the magnitude of heat generation rate due to oxidation is fixed for steam oxidation of zirconium; the magnitude of steam oxidation

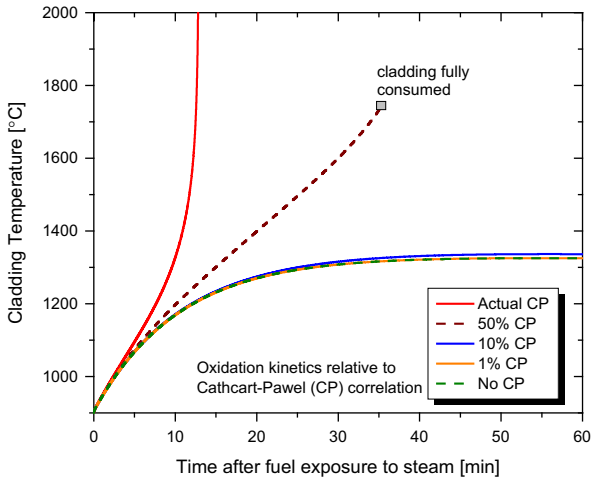

Fig. 8. Evolution in cladding temperature as a function of time with fuel rod exposed to 900 °C steam after 24 h of active cooling. The different curves correspond to various magnitudes of parabolic oxidation rate constant.

enthalpy for other materials such as iron alloys can be significantly lower. Fig. 8 shows that with an arbitrary 50% decrease in oxidation kinetics, the rapid temperature excursion in the cladding, though delayed and shifted up to higher cladding temperatures, still takes place in the absence of any cooling. However, if the oxidation kinetics are reduced by one or two orders of magnitude, the cladding temperature in this specific scenario will stabilize at 1300–1400 °C. This observation is specifically explained here by the fact that the power generation in the fuel (sum due to decay heat and oxidation) equilibrates with the magnitude of heat transfer from the fuel to the steam phase. The predictions in this simplified calculation are overly optimistic since the steam temperature is kept constant, and therefore an increase in cladding temperature increases the magnitude of the temperature gradient across the hydraulic boundary layer, consequently increasing the heat flux away from the cladding. However, the salient observation is that by lowering the heat generation rate associated with cladding oxidation, the minimum necessary heat removal rate from the fuel pins at high temperatures, required to avoid rapid temperature excursions, is reduced. In this manner, the slow oxidation reaction does not rapidly exacerbate the conditions in the core and the concomitant generation of hydrogen gas that increases the core pressure is also delayed and reduced.

Once high-temperature excursions in the fuel rod are avoided through utilization of materials that exhibit slower kinetics of oxidation, rapid heat and hydrogen production in the core could be potentially mitigated. Effectively, the critical heat removal limit for the entire core will be reduced to that of decay heat production inside the core, and any heat generation due to the oxidation reaction that can exacerbate this limit becomes negligible. Note that in case of short-term accidents (i.e., none or only a very short active cooling period is available), decay heat generation inside the core, even in the absence of the oxidation reaction, is sufficient to result in severe core degradation. An example of such a short-term scenario is the short-term station blackout (ST-SBO) in Fukushima Daiichi Unit1 (0.92 h after reactor scram) [52]. However, in other scenarios with longer term cooling periods, elimination of heat generation inside the core due to the oxidation reaction can alter the outcome of the accident in its entirety. An example of the latter is the long-term station blackout (LT-SBO) at Fukushima Daiichi Unit 2 that managed intermittent use of reactor core isolation cooling (RCIC) system until 66.8 h after reactor scram [52].

4. Historical application of steels as LWR cladding

In the initial days of LWR deployment, austenitic stainless steels were a popular choice for cladding material of UO_2 fuel pins for both experimental and commercial PWRs and BWRs [4,53–55]. The alloys utilized during the 1960–1975 time frame included Types 316, 304, 304L, and 347 stainless steels (both cold-worked and annealed), and nickel alloys such as Inconel 800 and Inconel 600 [4].

The earliest reported cladding failures occurred in the fuel pins of numerous BWRs. For example, intergranular cracking occurred in both annealed and cold-worked Type 304 cladding after only 500–1000 h of operation in the Vallecitos BWR [56]; further instances of intergranular cracking were encountered in fuel pin cladding in the Dresden-1, Big Rock Point, and Humbolt Bay BWRs [57,58]. The highly oxidizing water conditions in BWRs with $[O_2]$ on the order of ~8 ppm, an astonishingly high value by today's standards, were identified as a primary factor involved in the initiation of stress corrosion cracking (SCC). Other potential contributing factors included poor chemistry control (particularly phosphorus and silicon, which enhance grain boundary embrittlement), radiation hardening and early fuel pin designs, which produced high cladding stresses. The poor performance of stainless steel cladding in BWRs led to a relatively rapid switch to zirconium alloy cladding, which exhibited much lower fuel failure rates in early Generation I BWRs. Fig. 9 summarizes the observed fuel failure (clad breech) behavior for zirconium alloy and stainless steel cladding in BWRs and PWRs [4,59–63].

For the PWRs, a few early cases of intergranular cracking were observed in components of experimental PWRs and test loops. For example, intergranular cracking occurred in the annealed Type 304 cladding of burnable poison elements in the West Milton test loop at the Knolls Atomic Power Laboratory (KAPL), the failures resulted from internal stresses exceeding the yield strength in the presence of high concentrations of hydrogen [54]. Longitudinal cracks developed in the type 347 cladding in the PM-3A test reactor in the region of maximum neutron dose and internal stress, and in this instance cladding temperatures were high enough for hydrogen to be generated via localized boiling [58].

Apart from these observations of hydrogen-assisted cracking under extreme operating conditions of stress and temperature, the performance of thin-walled (0.25 mm) stainless steel cladding in the early PWRs was very satisfactory, with the lowest pin failure rate of any water-cooled reactor fuel [64,65], as shown in Fig. 9. For example, during six cycles of operation at Yankee-Rowe

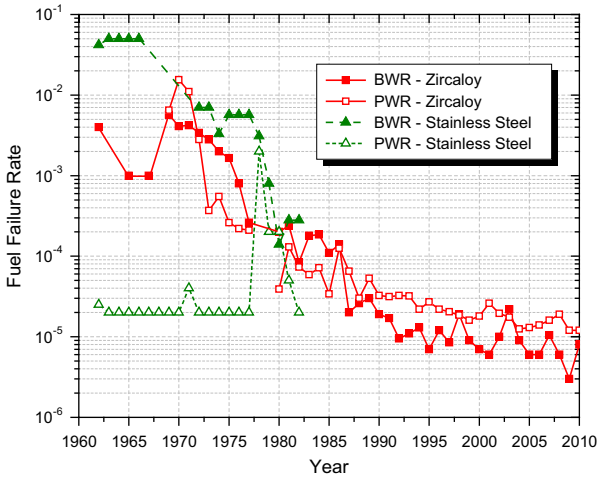

Fig. 9. Worldwide fuel performance history for Zircaloy and SS clad fuels in light water reactors [4,59–63].

(peak burnup of 45 GWd/MTU), only a single pin-hole cladding leak was detected. Similarly at Trino (Italy) [65] only one to two leaking fuel pins were detected during four operating cycles. At the Indian Point reactor, during four cycles between 1966 and 1973, not a single assembly of stainless steel-clad fuel pins was removed due to cladding leaks. Overall, the Westinghouse experience with stainless steel cladding in the period up to 1968 was that for a total of ~200,000 stainless steel fuel pins, the overall defect level was approximately 1 in 10^4 [66]. For comparison, the typical pin failure rate in zirconium alloy fuel in the early 1970s was about 0.1–0.3% for LWRs and CANDU reactors [64,67] (cf. Fig. 9).

Although the early observations of corrosion-related cracking in the stainless steel cladding exposed to BWR conditions were the source of considerable concern, this was eventually overshadowed by the issue of neutron economy. The thermal neutron cross section for stainless steel is a factor of ~12–16 times higher than that for Zircaloy, and the enrichment penalty incurred by the use of stainless steel cladding became the primary driver for the replacement of stainless steel cladding with Zircaloy cladding in commercial reactors after ~1970 (due to the acceptable fuel performance for Zircaloy cladding in both BWRs and PWRs, and gradual reductions in the fabrication cost for nuclear-grade Zircaloy tubing).

The early experiences with stainless steel in the BWR environment were instrumental in alerting the nuclear community to the existence of unexpected corrosion-related cracking mechanisms that could be encountered in light–water-cooled reactors. Subsequently, irradiation-assisted stress-corrosion cracking (IASCC) of core internals was encountered in a wide range of situations, and the international materials community embarked on an ongoing effort to understand the mechanisms involved and to develop strategies to circumvent the most damaging combinations of operating conditions, materials compositions, microstructural evolution, and stress conditions. A large number of mitigating variables have been identified including compositional variations, starting microstructure, yield strength, radiation-induced segregation, water chemistry, irradiation temperature, dose rate, and dose [68]. Moreover, significant advances were made in the control of reactor water chemistry. However, a full understanding of IASCC is confounded by heat-to-heat and specimen-to-specimen variability and the varying and complex nature of the radiation and chemical environment. Some important general findings were recently presented by Chopra and Rao [69,70].

Largely due to the impressive improvements in operating performance of zirconium alloy clad fuel systems in LWRs under normal operating conditions [3] during the past 35 years (Fig. 9), there have not been any significant research programs to investigate alternatives to the traditional 300-series stainless steels (18Cr, 8–12Ni) as potential high-performance materials for LWR cladding or reactor internals. However, within the fossil and other advanced energy programs significant advances have been made in high-strength, oxidation-resistant steels. Moreover, the discovery of the void swelling phenomenon in fast-reactor-irradiated Type 316 during the late 1960s led to the development of austenitic steels and ferritic–martensitic steels with properties tailored specifically for the neutron environment. In many respects, these advanced iron-based alloys could provide attractive alternatives to the conventional 300-series steels for application as fuel pin cladding materials in LWRs. From a strength, corrosion, and embrittlement standpoint, it appears that these advanced steels would enable fabrication of cladding with thinner walls than that of zirconium alloys, thus mitigating some of the neutronic penalty associated with their use.

5. Prospects for the utilization of advanced iron alloys in LWRs

Significant advances in both austenitic [71–73] and ferritic/martensitic [71,72,74–77] steels have been achieved over the past four decades since relatively simplistic austenitic steels were last used as a fuel cladding material in LWRs. The typical cycle time for the development of a new generation of steels is about 15 years [72,74], which translates into approximately three to four generations of improved austenitic steels compared to the Type 304, 316, and 347 stainless steels that were initially developed during the first half of the 20th century and subsequently utilized in Generation I LWRs in the 1960s. Along with the development of new steel compositions, dramatic improvements in commercial steel refining and casting methods have been introduced since the 1970s that enable better composition control and improved decarburization techniques. In parallel with this steady improvement in commercial steels, a remarkable improvement in the fundamental understanding of degradation mechanisms in steels such as SCC (including irradiation assisted, IASCC, mechanisms) [68,78–83] has occurred over the past 40 years; as noted in Section 4, stress corrosion cracking was the major fuel pin failure issue in the early Generation I reactors that utilized stainless steel cladding. Therefore it is appropriate to reexamine the suitability of advanced stainless steels (austenitic, ferritic, and martensitic grades) as potential high-performance and accident-tolerant candidates for LWR fuel cladding.

To facilitate the discussion of prospects for utilization of advanced iron alloys in LWRs, a review of fuel design criteria and guidelines imposed on the zirconium alloy cladding is appropriate. Design requirements for the fuel system are described in the NRC Standard Review Plan (SRP) Section 4.2 (NUREG-0800) [17] and are further manifested in other sets of federal regulatory codes [8,84–86]. The ultimate objectives of the fuel system design with respect to safety analysis are meant to ensure (a) the fuel system is not damaged as a result of normal operation and anticipated operational occurrences (AOOs), (b) fuel system damage is never so severe as to prevent control rod insertion when it is required, (c) the number of fuel rod failures is not underestimated for postulated accidents, and (d) coolability is always maintained inside the core. The fuel design evaluation process is a rigorous and iterative task and is to be performed by the fuel vendors with their choice of methodology. To perform such a comprehensive analysis for iron alloy cladding is well beyond the current scope. The goal of this paper is to simply point to the vast set of possible compositions and material options in the family of iron-based alloys that may be suitable for consideration as cladding. In the following, a brief review of properties of general alloy categories of interest along with a comparison with zirconium alloys is performed. Three major material properties are discussed: unirradiated mechanical properties, irradiation effects, and corrosion behavior.

5.1. Comparison of unirradiated mechanical properties

Given that unirradiated mechanical properties are largely the inputs to the fuel design evaluation analysis, these properties are briefly reviewed for iron alloys and compared to zirconium alloys. Specifically, unirradiated yield strength, relatively short-term creep rupture data, and Young's moduli are examined. Other important properties such as fatigue behavior, fretting resistance, or comparison of the wide range of thermophysical properties that are design inputs are not considered here.

Fig. 10 provides a side-by-side comparison of the temperature-dependent yield strengths of several alumina-forming ferritic alloys [87–89] as well as type 304 and 310 stainless steels [4,90] with zirconium alloys [91–96]. As shown in the figure, the yield

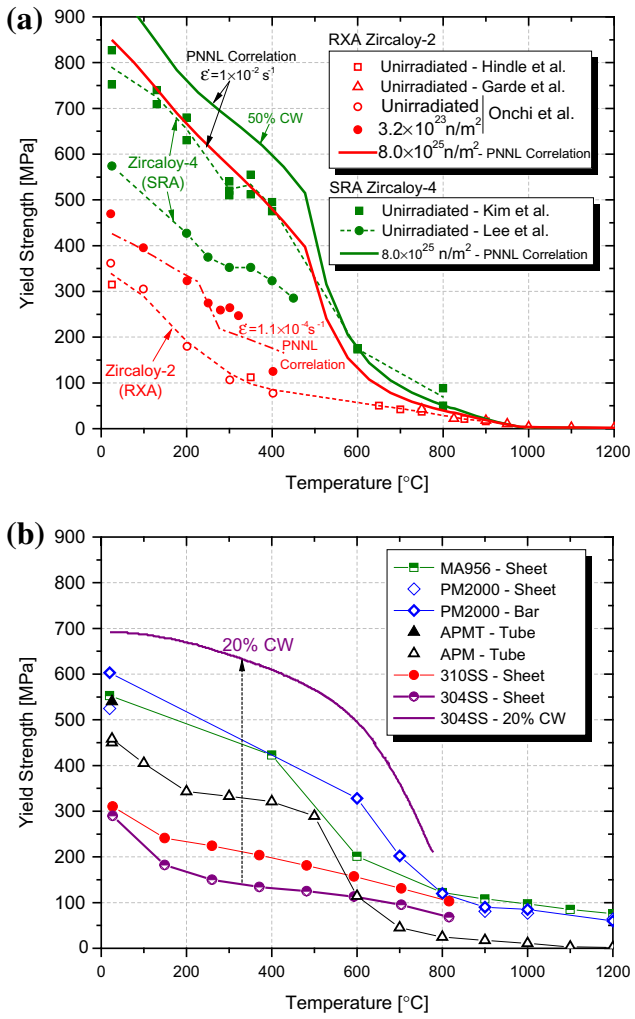

Fig. 10. Comparison of the elevated temperature unirradiated yield strength of (a) zirconium alloys and (b) several iron alloys [4,87–96]. Unless specified, the metals are in the fully annealed state.

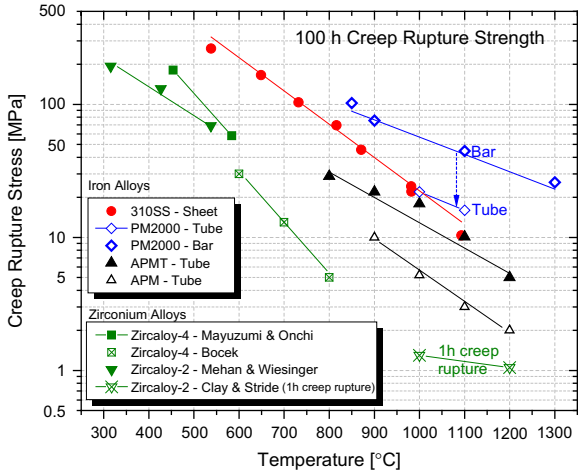

Fig. 11. Comparison of the 100 h high-temperature creep rupture strengths of iron alloys compared to Zircaloy-4 [87,89,106–110].

strength of unirradiated zirconium alloys spans a wide range of values. This is largely dominated by the thermomechanical treatment (TMT) of the cladding during fabrication (via pilgering), which results in various grain sizes and degrees of cold-working and recrystallization in the alloy [97]. Alloy composition (e.g., the oxygen content) also affects this property. For instance Zircaloy-2 used for BWR applications, given corrosion considerations, is used in the recrystallized (RXA) state with yield strength at the lower end of the spectrum, as observed in Fig. 10. In contrast, the Zircaloy-4 in PWRs in the stress-relieved annealed (SRA) condition exhibits much higher yield strength. This contrast coupled with the larger diameter of the BWR fuel pins results in thicker cladding requirements in BWR bundles based on the fuel design evaluation process. It is worth noting that regardless of the initial metallurgical state, the yield strength of different irradiated zirconium alloys increases to reach similar values after a modest fast neutron fluence of $\sim 1 \times 10^{24}$ n/m^2 and in effect saturates at that value [98,99]. This is shown in Fig. 10 for RXA Zirclaoy-2 and SRA Zircaloy-4 with 50% cold-work using PNNL yield strength correlation [96] at a fluence of 8×10^{25} n/m^2. The yield strength of irradiated cladding drops rapidly at $T > 600$ °C, due to damage recovery via thermal processes, to reach that of unirradiated zirconium alloys.

Just as TMT, alloy composition, and microstructure affect the mechanical properties of zirconium alloys, the same is true for iron-based alloys. All the alumina-forming FeCrAl alloys in Fig. 10 are ODS variants (MA956 and PM2000) except the APM variant, which shows a lower yield point at room temperature. Significantly higher yield strength values for PM2000 bar with a different microstructure from the alloy in Fig. 10 are reported elsewhere [100]. Similarly, the yield strength for 310SS in Fig. 10 is for a fully annealed material. Considering the significant degree of work hardening inherent to austenitic steels prior to necking, introduction of cold-working is expected to increase the yield strength (but limit ductility). This is shown in the figure by comparison between the annealed and cold-worked (CW) 304SS.

The feasibility of using significantly thinner iron alloy cladding than what is currently utilized in zirconium alloy cladding LWR fuel systems, in order to partially compensate for the higher neutron absorption cross sections in the former, needs to be examined. The viability of thinner steel cladding was demonstrated in the 1960s and 1970s era stainless steel cladding [4,101]. A full evaluation of the potential optimized steel cladding thickness would need to consider corrosion, grid-to-rod fretting, and other cladding reliability issues. However, from a simple cladding yield strength standpoint (Fig. 10), given potential improvements by alloy optimization, steel cladding with significantly reduced thickness compared to the current zirconium alloy cladding may be anticipated. Also note that the thickness loss due to oxidation in zirconium alloys (Figs. 4 and 7) is expected to be significantly less for iron-based alloys; this in turn also reduces the requirements on the initial cladding thickness.

For LOCA conditions, an important strength property is short-term creep rupture strength. During a LOCA, zirconium alloy cladding experiences burst in the temperature range of ~700–1100 °C (spanning over the $\alpha \rightarrow \beta$ transition point) due to the pressure differential present from the cladding internal volume to the depressurized core environment [102]. Zirconium alloy cladding burst has been modeled extensively [103,104] and is dominated by cladding creep at those temperatures. After rod burst, maintaining coolable core geometry is another important regulatory requirement and has also been examined extensively. The results from the RE-BEKA tests ultimately showed that flow blockage up to 90% does not compromise coolability [105]. Fig. 11 summarizes 100 h thermal creep rupture strength data for a similar set of materials as Fig. 10. Despite its higher melting temperature than steels, the high-temperature short-term creep rupture strength of Zircaloy-4 is lower than many of the iron alloys and it is further reduced once hydrogen is absorbed into the alloy [12]. Conservative values, associated with tube and sheet materials, have been used for iron alloys

since for instance in ODS FeCrAl alloys the larger grain size in bar specimens enhances the rupture strength by about an order of magnitude. Note that the 3%Mo addition in APMT significantly enhances creep resistance compared to the APM variant. Both alloys have quasi-ODS strength due to the coarse oxide dispersion formed via the advanced powder metallurgy (i.e. APM) processing. Higher creep resistance can facilitate thinner iron alloy cladding and enhance the burst margins under LOCA scenarios as was previously demonstrated by 304SS type cladding [106].

Zirconium alloys have a relatively low elastic modulus (more flexing for a given applied stress), which may exacerbate grid-to-rod fretting issues associated with coolant-flow-induced vibrations of the fuel assembly against the grid support plates. Young's modulus for various zirconium alloys and along different crystallographic orientations has been studied and reported [111,112]. As shown in Fig. 12, the Young's modulus for zirconium alloys [96] is roughly half the corresponding values for the iron alloys discussed here over a broad temperature range.

5.2. Irradiation effects on iron alloys for cladding application

A second important consideration is radiation effects on the proposed iron alloy cladding systems. There is a broad database on the effects of LWR irradiation on the mechanical and physical properties of austenitic [68–70,113–118] and ferritic/martensitic steels [74,119–126]. Overall, irradiation effects are not anticipated to produce unacceptable property degradation for cladding applications. At normal LWR cladding operating conditions (T_{irr} ~ 300 °C and doses up to ~15 dpa), the major radiation-induced changes are associated with radiation hardening and embrittlement. Neutron irradiation under these conditions can cause the yield strength to quadruple for austenitic steels [113] and double for ferritic/martensitic steels [125] compared to their unirradiated value at 300 °C. The corresponding uniform elongation can decrease to values below 1% due to radiation hardening and plastic flow localization phenomena during fission neutron irradiation near 300 °C [127]. This reduction in uniform elongation in both austenitic and ferritic/martensitic steels occurs after irradiation to damage levels of several dpa; the reduction is somewhat more pronounced in ferritic/martensitic steels. The hardening and embrittlement for LWR cladding conditions is mainly due to formation of dislocation loops and helium-containing cavities for austenitic stainless steel [113] and dislocation loops and precipitates for ferritic/martensitic steels [119,128].

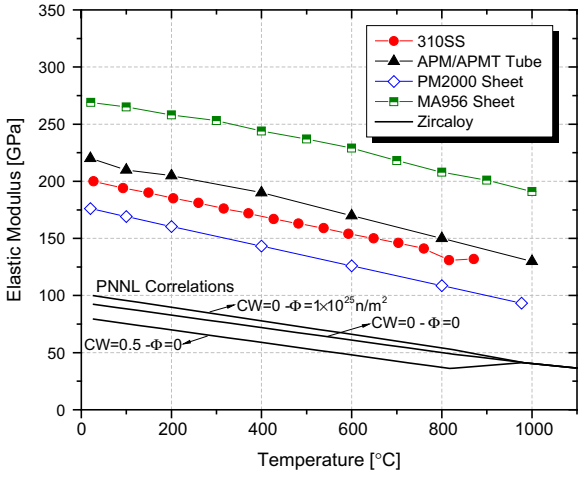

Fig. 12. Temperature-dependent elastic moduli for ODS FeCrAl alloys, 310SS, and Zr alloys [87–89,96].

Phase instabilities associated with α–α′ phase decomposition and the potential for accompanying embrittlement (historically known as the 475 °C embrittlement issue) is a significant concern for ferritic steels with Cr contents over ~9% [129–131]. At <475 °C, there is insufficient solute mobility for pronounced α′ embrittlement, and at higher temperatures even higher chromium levels can be used without alpha′ embrittlement concerns due to increased chromium solubility. The radiation-enhanced diffusion during neutron irradiation near 300–400 °C can produce significant alpha' precipitation and embrittlement for matrix chromium levels > 7% Cr, which corresponds to overall chromium concentrations > 9%Cr (since 1–2% of the chromium is typically associated with carbide precipitates purposefully formed during tempering) [128]. Considering that chromium contents above ~9%Cr are needed to provide good oxidation resistance during prolonged exposure to water or steam, ferritic/martensitic steels with ~9% Cr are a good compromise between oxidation resistance and radiation embrittlement (α′ decomposition) resistance. According to calculated phase diagrams [132], the addition of Al does not suppress the driving force for decomposition. Experimental results from PM2000 (ODS FeCrAl) alloys annealed at 450–480 °C showed clear α′ formation [133]. Potential embrittlement in steels associated with hydrogen pickup is a minor issue compared to the situation for zirconium alloy cladding, owing to relatively low hydrogen solubility in steels [134,135].

In general, fracture toughness is not as important for cladding (compared to reactor pressure vessel applications) due to the plane stress loading conditions associated with thin wall tubing. Fracture toughness is reduced in both austenitic [69,113,114] and ferritic/martensitic [74,119–125] steels after neutron irradiation near 300 °C. However, experimental results indicate fracture toughness values of at least ~50 MPa $m^{1/2}$ should be maintained at the cladding operating temperature for irradiation doses up to at least ~20 dpa. Zircaloy-2 and -4 suffer pronounced reduction in ductility and fracture toughness as a result of both irradiation hardening and hydride precipitation. Uniform elongation on the order of 1–5% and total elongation up to 20% have been observed for Zircaloy fuel rod cladding upon discharge [136,137]. For irradiated zirconium alloy cladding with modest hydrogen content fracture toughness, values on the order of 20–50 MPa $m^{1/2}$ are expected [138]. The fracture toughness in irradiated Zircaloy falls to 12–15 MPa $m^{1/2}$ if hydrogen concentrations approach 1000 wt ppm.

Dimensional changes due to void swelling or irradiation creep in austenitic [117,118] and ferritic/martensitic [119,126] steels are not expected to be of concern for LWR cladding conditions (~300 °C, 15 dpa). The anticipated amount of dimensional change based on experimental studies would be <1% and isotropic in nature. This was specifically showed for a Fe–22Cr–5Al–0.7Y alloy irradiated up to 100 dpa [139]. Iron alloys will not be susceptible to pronounced irradiation growth that is observed in zirconium alloys. This phenomenon occurs in zirconium alloy cladding tubes due to the combination of anisotropic crystal structure and grain orientation (texture) [140].

5.3. Corrosion considerations under normal operating conditions

The third major area to be evaluated is the corrosion behavior of iron-based alloy cladding structures under normal operating conditions in LWRs. There is significant LWR operating experience on the behavior of austenitic stainless steel structural components that have been in service for multiple decades [68,70,78–82]. Although the operating temperatures (280–290 °C) for these components are slightly lower than the cladding, the generally favorable performance of austenitic core internal components during decades of reactor operation suggests that corrosion and dissolution issues would not be significant. It should be recognized that

the water chemistry trends and degradation management strategies have evolved tremendously, resulting in current environments drastically different from those up to the 1970s. Groundbreaking strategies such as strict control of pH and chemistry, hydrogen water chemistry (HWC), zinc additions, and cyclical, and subsequently online, Noble metal chemical addition (NMCA) procedures in BWR and PWRs have resulted in a drop in oxygen potential by at least an order of magnitude. Accordingly, significant drops in corrosion potentials are achieved that fundamentally mitigate susceptibility to SCC among other degradation mechanisms involving corrosion.

IASCC that is observed in austenitic steels exhibits a well-known dose threshold. The relatively limited dose requirements (~15 dpa) for cladding applications along with the significant drops in oxygen potentials alleviate many of the IASCC concerns. Also, a transition away from 18–8 alloys to alloy compositions that are potentially less susceptible has been made [68,70,78–80,82].For ferritic alloys with sufficient Cr, corrosion in water or steam at normal LWR operating conditions would not be expected to be of concern. For example, the uniform corrosion rate of 9% Cr ferritic/martensitic (a relatively low chromium content in the context of the current discussion) steels in an aggressive environment of supercritical pressurized water at 550 °C is less than 0.04 mm/year [141]. Stress corrosion cracking of ferritic steels is generally much less of a concern than in austenitic steels. Note that for the FeCrAl class of alloys, the formation of an alumina film at the surface under normal operating temperatures is not expected and passive protection is attributed to the presence of a chromia film. Pre-oxidizing the cladding, as sometimes is performed on the lower sections of zirconium alloy cladding, is not deemed appropriate for FeCrAl alloys. Typically, temperatures >600 °C will be necessary to produce an alumina scale. The scale is then susceptible to wear or dissolution under normal operating conditions under which the alumina scale will not reform. Radiation-induced segregation of chromium under irradiation in ferritic alloys is not considered to be an issue from the corrosion standpoint. However, it could be a concern for grain boundary embrittlement or to initiate phase instabilities.

5.4. Tritium transport

Tritium is produced via a multitude of pathways in LWRs, but largely the production volume is dominated by ternary fission in nuclear fuel (with a yield of $\sim 10^{-4}$ per fission) and neutron absorption by boron in the PWR primary coolant [4,142,143]. The amount of tritium released from the fuel pellet into the cladding internal volume is independent of the cladding type. However, the release fraction from the historic 304SS and Zircaloy cladding differs widely where the value resides at ~50% and ~1%, respectively. This is largely due to the strong chemical affinity of zirconium for isotopes of hydrogen [144]: essentially the zirconium, which in the process embrittles, serves as tritium storage medium.

Tritium released into the primary coolant rapidly reacts with radiolysis products to form HTO and largely resides in the coolant water. In current PWRs, tritium released from the fuel is on the order of 10% of the total tritium content into the primary coolant; the rest is due to the $^{10}B(n,2\alpha)^{3}H$ reaction. An increase in tritium release from the fuel with iron-based cladding can rival the extent of production as a result of neutron absorption by boron in PWRs. In BWRs, where the sole significant source of ^{3}H is the fuel, a small fraction of tritium can be transported to the turbine via the gaseous phase. Therefore, any increase in the extent of release from the fuel will be directly proportional to the increase in the overall plant dose. Note that hydrogen permeability of bcc iron alloys is known to be higher than fcc variants [145]. The environmental and plant management aspects of such an increase are beyond the scope of this manuscript but deemed largely inconsequential given the prior experience with steel cladding and modern radionuclide release management strategies from the core to the turbine in BWRs.

6. Reactor physics and economic aspects of iron-based alloy cladding

Following high temperature steam oxidation behavior and expected materials performance under normal operating conditions, two essential areas remain that need to be addressed for iron based alloy cladding systems for LWR fuel elements: reactor physics and economics. Though a neutronic penalty upon the transition to iron based alloy cladding materials is expected, it is important to quantify its magnitude and discuss alternate fuel design configurations that reduce it. The magnitude of this penalty directly impacts fuel economics that in turn needs to be examined and quantified to serve informed and complete discussions on the viability this fuel concept.

6.1. Reactor physics

A simplified single-pin (a single fuel rod) reactivity analysis has been performed providing a comparison between current zirconium-alloy-clad oxide fuel bundles and those with iron alloy cladding using the TRITON module from the SCALE 6.1 package [146]. The details of the calculations are discussed and extensive results are provided elsewhere [147]. Briefly, calculations were performed with the ENDF/B-VII cross-section library using 238 energy groups. Two-dimensional transport calculations were performed with the NEWT transport code, which is coupled with ORIGEN-S to perform depletion in the fuel as well as the cladding. The reference case in the following calculations is that of a PWR 17 × 17 fuel bundle with 4.9% enriched urania pellets, as shown in Table 1. Currently high-power-density plants in the United States use 4.6–4.9% enriched fuel [148]. The UO_2 fuel pellet density was fixed at 96% of theoretical density (10.47 g/cm^3). The same alloys identified for the analysis in Section 3, the base FeCrAl alloy and 310 stainless steel, were selected. The alloy compositions are listed in Table 2.

Fig. 13 shows the evolution in infinite multiplication factor (k_{inf}) as a function of effective full power days in fuel rods at the standard PWR 17 × 17 geometry with various cladding materials. A clear neutronic penalty is shown associated with utilization of the steel cladding materials owing to the larger neutron absorption cross section in these materials. The reactivity penalty in case of the ferritic FeCrAl alloy is less than that of 310SS owing to the absence of nickel in this material. Nickel exhibits a thermal neutron absorption cross section roughly twice that of iron. Meanwhile, the presence of nickel results in production of radioactive cobalt via the $^{58}Ni(n,p)^{58}Co$ reaction. At a constant core power density, this drop in reactivity corresponds to a significant reduction in operational cycle length. Therefore, modified bundle geometries with iron-based alloy cladding materials are necessary to enhance their reactivity and enable them to achieve similar cycle lengths as that of the reference bundle design with Zircaloy cladding.

To conserve cycle lengths at constant operational power, the end-of-cycle (EOC) reactivity needs to be maintained constant at what is achievable for reference fuel bundles. To enhance the

Table 1
Reference PWR 17 × 17 fuel bundle geometry [149].

Pellet OD (mm)	8.192	Clad thickness (μm)	572
Pellet-Clad Gap (μm)	83	Pitch-to-diameter	1.326
Clad ID (mm)	8.357	UO_2 mass per assembly (kg)	611
Clad OD (mm)	9.500	Zircaloy clad mass per assembly (kg)	125

Table 2
Composition in mass fraction (wt%) of evaluated cladding materials.

Alloy	Fe	Cr	Al	Zr	Ni	Sn	Mn	Mo	Si	σ_a[a] (barns)
FeCrAl	75	20	5	0	0	0	0	0	0	2.43
310SS	52.5	25.2	0	0	19.5	0	1.9	0.13	0.7	3.21
Zircaloy-4	0.15	0.10	0	98.75	0	1.50	0	0	0	0.20

[a] Average thermal neutron absorption cross section for the alloy.

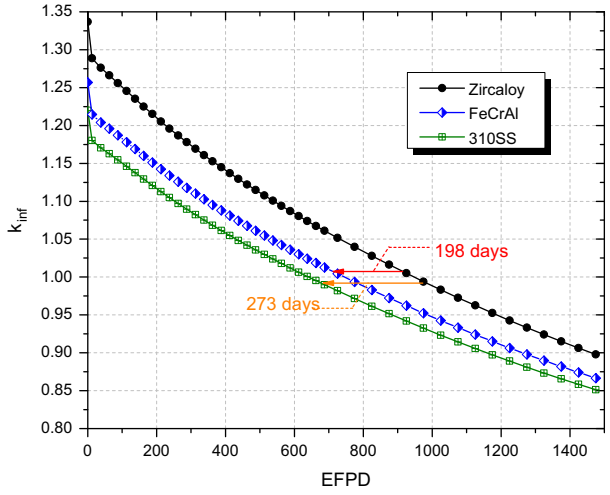

Fig. 13. k_{inf} versus effective full power days in fuel rods at the standard PWR 17 × 17 geometry with various cladding materials.

EOC reactivity in bundles with iron-based alloy cladding, three separate approaches can be considered: increase the fuel enrichment, minimize the clad thickness, or increase the fuel mass inside the core. The first implies that the current geometry for the fuel bundle is conserved while the fissile material density per unit volume of the core is increased by increasing the ^{235}U enrichment. The second and third are coupled in that as the clad thickness is reduced, for a given gap, that surrendered space can accommodate additional fuel while fixing ^{235}U enrichment at a constant value. Note that the outer diameter, fuel clad gap, and the pitch-to-diameter ratio of the fuel rods are fixed at the standard PWR 17 × 17 geometry to avoid the need to consider thermal hydraulic complexities. It is worthwhile to note that yet another approach, although ignored here, is to increase the fuel pellet stack height in the rod. This was in fact a method used for the Connecticut Yankee Nuclear Power Plant (CYNPP) when it utilized 304L stainless steel as fuel cladding [101]. The fuel stack height for the 304L clad rods were roughly 1.6% taller when compared to the rods with Zircaloy-4 clad and the clad thickness was substantially less (nominally 419 μm steel compared to 686 μm Zircaloy). Use of stainless steel cladding as thin as 300 μm has been reported [4]. The ability to use thinner clad would be enabled both by the higher strength of the steel and by its enhanced corrosion performance (retained strength with operation) as discussed in Section 5.1. The reduced steel thickness (and stack height) not only mitigated the neutronic scavenging impact of the clad but enhanced the overall core fuel loading substantially (411.5 kg U/assembly for the steel clad compared to 363.8 kg U/assembly for the Zircaloy).

Fig. 14 shows the contour map of the variation in EOC Δk_{inf} against the benchmark Zircaloy-clad UO_2 fuel (the benchmark case is fuel geometry specified in Table 1 with 4.9% enrichment). A three batch scheme was used during this analysis and details are reported elsewhere [147]. The EOC Δk_{inf} is mapped as a function of both cladding thickness and fuel enrichment to combine the two approaches detailed earlier. When the difference in EOC infinite multiplication factors is zero, the implication is for identical cycle lengths to the benchmark case. Given the inherent assumption in all these calculations that core output power is constant, positive and negative deviations in EOC Δk_{inf} correspond to longer and shorter cycles, respectively. Reduction in cladding thickness to ~300 μm with its associated increase in fuel pellet diameter at constant fuel enrichment of 4.9% is necessary to maintain the current cycle lengths, assuming no stack-height or other geometric change. At the alternate extreme, by maintaining the existing (Zircaloy-based) geometry and solely increasing fuel enrichment, an increase of ~1% in ^{235}U content is necessary. In reality, given that the previous (circa 1970) state of the art utilized a rather low-performance, 419 μm steel, it would be assumed that a present-day clad could be significantly thinner than the 419 μm steel cladding used in CYNPP, combined with some stack height adjustment potentially eliminating the need for increased enrichment. In any event, only modest enrichment above today's standard is anticipated.

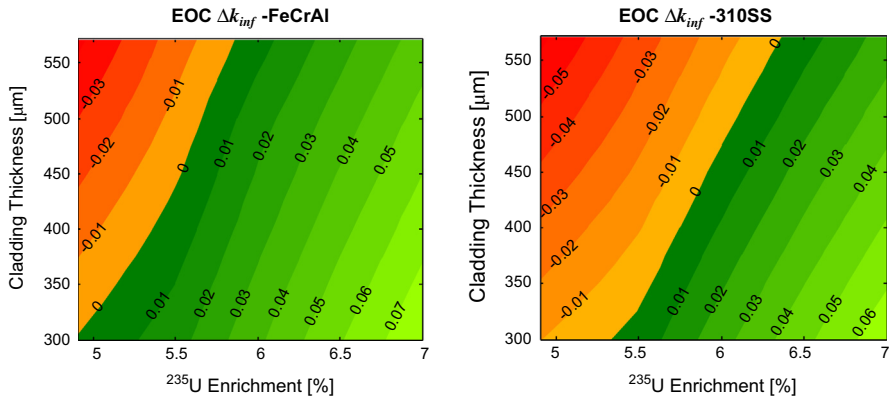

Fig. 14. EOC infinite multiplication factor difference against benchmark Zircaloy clad fuel as a function of cladding thickness and fuel enrichment for FeCrAl and 310SS clad fuel.

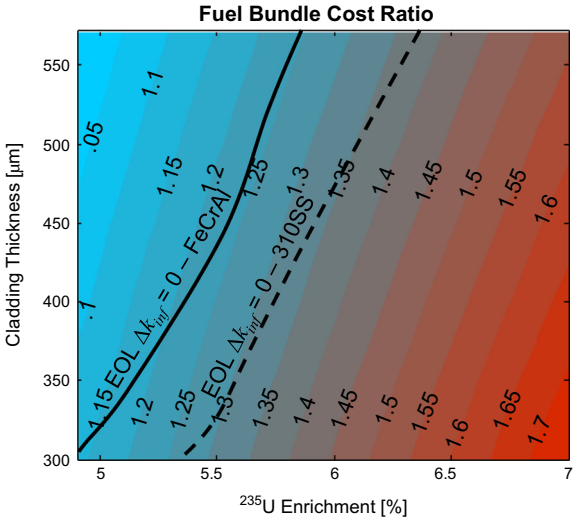

Fig. 15. Increase in fuel bundle cost as a function of iron alloy cladding thickness and fuel enrichment.

6.2. Economics

The magnitude of increase in the fuel bundle cost due to the increase in the required low enriched uranium (LEU) mass (i.e., larger pellets) and higher enrichment in the fuel is necessary to estimate the impact on the economics of nuclear electricity production upon adoption of iron-based alloys as nuclear fuel cladding. The consideration here is limited to oxide fuel pellets, and it is assumed that the fabrication cost of pellets is independent of the enrichment and geometry (variation in the diameter) of the cylindrical pellet. Note that the cost of retrofitting current oxide fuel fabrication facilities to accommodate slightly higher enrichment uranium is not considered here. Also any reduction or increase in cost by switching from zirconium alloy to iron-based alloy cladding is similarly ignored. The analysis used to estimate the increase in fuel bundle cost as a function of increase in low enriched uranium (LEU) mass and enrichment is detailed in Appendix B. Fig. 15 shows the magnitude of increase in normalized assembly cost (against the reference design at 4.9% enrichment) as a function of cladding thickness and enrichment. Superimposed on this figure are the lines from Fig. 14 that correspond to the zero EOC Δk_{inf} between the iron and zirconium alloy clad bundles. The increase in fuel bundle cost for the iron alloy cladding is estimated to be on the order of 15–35% when compared to the current zirconium alloy/urania fuel bundles.

From an economic standpoint and ignoring mechanical integrity requirements, given the findings in Fig. 15, the preferred route to enhance reactivity in the iron-based alloy clad assemblies is to minimize the cladding thickness. As was discussed, iron-based alloys offer higher strength and therefore a significant reduction in cladding thickness compared to existing zirconium alloy cladding appears feasible. The cladding outer diameter in both cases was 10.72 mm. Meanwhile, note that fuel costs in the US commercial nuclear power fleet comprise 28% of the electricity production cost [150]; the rest are attributed to operations and maintenance (O&M). As shown in Fig. 15, upon adoption of iron-based alloy clad fuel, an increase in fuel costs between 15% and 35% is expected. Accordingly, an increase on the order of 4–10% in the total electricity production cost is to be expected (ignoring retooling costs for cladding fabrication, and assuming comparable fuel failure rates).

7. Conclusions

The following conclusions are drawn given the discussion provided in this manuscript:

1. Zirconium alloys are fundamentally susceptible to severe degradation under beyond-design-basis-accident conditions. The chemical and physical degradation processes in the core during an accident sequence are considerably exacerbated by rapid oxidation of zirconium alloys at $T > 1200$ °C.
2. Advanced iron alloys offer potential for improved oxidation resistance (reduced hydrogen generation) and improved strength compared to existing zirconium alloy cladding up to at least 1300 °C; both of these attributes are desirable in terms of improved accident tolerance and would favorably contribute to increased coping time in a beyond-design-basis-accident scenario.
3. Though iron-based alloys have enjoyed decades of active R&D across various disciplines, targeted research is necessary to evaluate the application of advanced variants of alloys from this family for LWR cladding and develop scalable alloy designs optimized for this application. Particularly, stress corrosion cracking behavior (including irradiated-assisted effects) and other embrittlement and degradation processes for candidate alloys in LWR environments need to be examined. In similar manner, integral LOCA and RIA behavior of these fuel structures needs to be evaluated.
4. Assuming fixed cladding and fabrication costs, The increased UO_2 mass or increased ^{235}U enrichment needed to offset high neutron absorption by the iron alloy cladding would result in a modest (~4–10%) increase in electricity production costs, ignoring retooling costs and assuming comparable fuel failure rates.

Acknowledgments

The authors would like to extend their gratitude to Larry Ott, Kevin Robb, and Graydon Yoder in the Reactor and Nuclear Systems Division as well as Bruce Pint and Sebastian Dryepondt in the Materials Science and Technology Division at ORNL for their technical insight. Thoughtful discussions and guidance received from Robert Montgomery at PNNL and Dion Sunderland at Anatech Corp are also gratefully acknowledged. The work presented in this paper was supported partially by the Advanced Fuels Campaign of the Fuel Cycle R&D program in the Office of Nuclear Energy, U.S. Department of Energy as well as by Laboratory Directed R&D funds at ORNL.

Appendix A. Fuel/cladding temperature evolution calculation

A simplified analysis is used, adopted after Olander [28], where the radial distribution of temperature in the fuel and cladding, oxygen diffusion profile into the cladding, and oxidation of the cladding in contact with the fuel have all been ignored. The first assumption is effectively inconsequential to this analysis since the magnitude of the temperature gradients in the fuel and cladding due to decay heat generation is very small (~5 K/mm) in the absence of the fission reaction. The latter two assumptions introduce only negligible errors in the calculation as well. The simplified transient heat equation in the fuel is given by

$$(\pi R_F^2)(\rho C_p)_F \frac{dT_F}{dt} = LHR_{decay} - (2\pi R_F) h_{FC}(T_F - T_C). \quad \text{(A1-1)}$$

R_F, ρ, C_p, and h_{FC} are the fuel radius, density, heat capacity, and the thermal conductance between the fuel and cladding, respectively. The product of ρ and C_p is the volumetric heat capacity, and its value for the urania fuel pellet in this calculation is assumed constant at 3.2 J/cm^3 K. While the temperature dependence of this parameter can be captured via detailed correlations provided elsewhere [151], it is ignored here since it only experiences a variation of ±10% in the wide temperature range examined here. h_{FC} is governed by the nature of fuel-cladding contact and is a function of burnup; its magnitude can span a wide range. In this analysis a value of 0.03 W/cm^2 K, representing a very poor state of conductance, is assumed, although much larger values (up to 2 W/cm^2 K) can be the case if the fuel is tightly bonded to the cladding [23,152]. The exact magnitude of this value happens to be irrelevant to the results of this analysis since heat transfer phenomena in the fuel and cladding have a much larger dependence on the cladding-to-steam heat conductance. The latter is at least two orders of magnitude smaller than h_{FC}; evident of the near-adiabatic conditions in the fuel during LOCAs. LHR_{decay} is the linear decay heat production in the fuel that is a function of time after reactor scram. A good approximation for LHR_{decay}, ignoring the negligible effect of burnup on short-term decay heat generation rate [153], is provided as [154]

$$LHR_{decay} = 9.5 \times 10^{-2} LHR_{\circ}(t + t_{\circ})^{-0.26}. \tag{A1-2}$$

The above equation implies that instantaneously after reactor scram, the LHR_{decay} is 9.5% of the LHR during normal operating conditions ($LHR_{\circ}$). Also, its value decays as a function of time with the power dependence specified. $t_{\circ}$ is the time elapsed from the onset of reactor scram up to the point that marks the start of the oxidation analysis. More sophisticated methods to estimate decay heat production in the fuel [155], although available, have not been used in the current simplified model that is intended to convey general trends in fuel assembly response, but could be utilized in the future in a more sophisticated computational model.

In a similar manner to what was described for the fuel pellet, the transient heat equation in the cladding is written as

$$(2\pi R_C \delta_C)(\rho C_p)_C \frac{dT_C}{dt} = LHR_{ox} + (2\pi R_F) h_{FC}(T_F - T_C) - (2\pi R_C)\bar{h}(T_C - T_{st}). \tag{A1-3}$$

R_C, δ_C, $\bar{h}$, and T_{st} are the cladding outer radius, cladding thickness, heat conductance term between the cladding outer radius and steam, and steam temperature, respectively. T_{st} is assumed to be a constant value of 900 °C; indeed, this is the most simplistic assumption in this analysis. Note that the radiation heat transfer mechanism has been ignored altogether in this simplified analysis. The volumetric heat capacity (ρC_p) in the cladding is assumed to be fixed at 2.3 J/cm^3 K. This assumption ignores the variation in this parameter upon α–β phase transformation in the zirconium alloy cladding at ~900 °C and once the oxide phase has formed. LHR_{ox} is the linear heat generation rate due to enthalpy production as the cladding oxidation proceeds and is given by

$$LHR_{ox} = 2\pi R_C \rho_{zr} H \left(\frac{dl}{dt}\right), \tag{A1-4}$$

where ρ_{zr}, H, and l are the zirconium density in the oxide phase (4.2 g/cm^3), energy of formation of zirconium oxide per unit mass of zirconium as a result of steam oxidation (6.45×10^3 J/g), and oxide layer thickness, respectively. Given that the kinetics of the zirconium oxide layer growth is controlled by oxygen diffusion through the oxide layer (parabolic kinetics), the oxide layer thickness as a function of time at constant temperature is given by

$$l^2 = \left(\frac{k_{ox}}{\rho_{ox}}\right)^2 t + l_{\circ}^2. \tag{A1-5}$$

ρ_{ox} is the density of oxygen in the zirconia layer (1.48 g/cm^3), and $l_{\circ}$ is the initial oxide layer thickness. k_{ox}, as was discussed in Section 3, is the parabolic rate constant of the zirconium oxidation reaction in steam. Using the Cathcart–Pawel correlation [42], the k_{ox} in g/cm^2 s$^{1/2}$ is given as

$$k_{ox} = 6.02 \times 10^{-2} \exp\left(\frac{-83.6\ [\text{kJ}]}{RT}\right). \tag{A1-6}$$

One can define the parabolic oxidation parameter K as

$$K = \left(\frac{k_{ox}}{\rho_{ox}}\right)^2. \tag{A1-7}$$

The rate of oxide layer growth at any temperature is then given by

$$\frac{dl}{dt} = \frac{K}{2\sqrt{Kt + l_{\circ}^2}}. \tag{A1-8}$$

Therefore the LHR of oxidation at any constant temperature and as a function of time at that temperature, given an initial oxide layer with thickness of $l_{\circ}$, is determined by

$$LHR_{ox} = \pi R \rho_{zr} H \frac{K}{\sqrt{Kt + l_{\circ}^2}}. \tag{A1-9}$$

Using Eq. (A1-9), LHR_{ox} is calculated at each time step given the calculated oxide thickness and temperature. Given these simplified equations and set of parameters, a numerical approach is used to calculate the evolution in the fuel and cladding temperature after the core becomes exposed. The numerical method utilized here is that of the explicit Euler's route with sufficiently short time-steps (0.01 s) to minimize the error in the solution.

Appendix B. Increase in fuel cost as a function of an increase in LEU mass and enrichment

Fuel cost (FC) is composed of two components of uranium and fabrication costs as follows:

$$FC = U + F_f. \tag{A2-1}$$

The uranium related costs, U, consist of four components:

$$U = U_m + U_c + U_d + U_e, \tag{A2-2}$$

where subscripts m, c, d, and e denote uranium milling/mining, uranium conversion, depleted uranium (DU) disposal, and uranium enrichment, respectively. F_f represents the fuel fabrication cost that is on the order of $250 and $300 per kg of LEU for PWR and BWR fuel, respectively [156]. Assuming fabrication costs remain unaltered, the uranium costs can be somewhat accurately calculated given the final mass of LEU in the fuel bundle and its enrichment level. Uranium milling/mining, conversion, enrichment, and DU disposal are commercially available services with a known market price (albeit variable with time). The required mass of natural uranium feedstock per fuel bundle, mass of depleted uranium to be disposed, and the separative work unit (SWU) can all be calculated using the well-developed theory of uranium enrichment [157]. The SWU required for an enrichment process that feeds in mass F of uranium at enrichment x_F and produces an LEU mass of P with x_P enrichment leaving behind mass T of DU waste with x_T fraction of remaining ^{235}U is given by

$$SWU = P \cdot v(x_P) + T \cdot v(x_T) - F \cdot v(x_F), \tag{A2-3}$$

where the value function $v(x)$ is given by

$$v(x) = (1 - 2x)\ln\left(\frac{1 - x}{x}\right). \tag{A2-4}$$

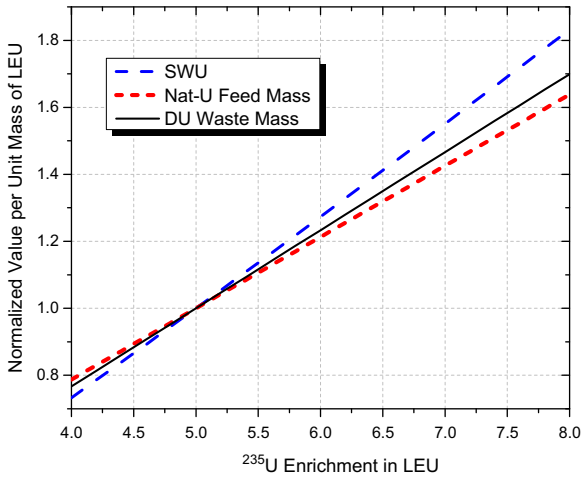

Fig. 16. Necessary SWU, natural uranium feed and depleted uranium stream mass per unit mass of LEU as a function of ^{235}U enrichment in LEU stream.

Using this methodology, Fig. 16 shows the variation across the required initial natural uranium feed, the depleted tailings stream mass, and the SWU required per unit mass of LEU at different enrichment levels. The U-235 content in the natural uranium feed and inside the depleted uranium waste stream are assumed to be 0.711% and 0.3%, respectively. All the values are normalized against that of the case for 5% U-235 enrichment.

The variation in the normalized values shown in Fig. 16 could be used in conjunction with the set of cost parameters from a reference fuel bundle to calculate the costs of new UO_2 fuel bundles with larger pellet diameters and enrichments. The reference fuel bundle considered here is the AP-1000 17 × 17 PWR fuel assembly. Given the LEU mass per bundle (Table 1) and assuming 4.9% fuel enrichment, Eq. (5) can be used (along with the law of conservation of mass) to calculate the required mass of natural uranium (Nat-U), the magnitude of the DU stream, and the extent of SWU for the reference bundle. Accordingly, 538 kg of LEU at 4.9% enrichment in the reference bundle requires 6031 kg of Nat-U feed, results in 5492 kg of DU tailing stream, and inputs 3774 SWU. The total assembly cost is estimated using the uranium mining/milling priced at $75/kg of Nat-U, uranium conversion at $10/kg of Nat-U, enrichment at $110/SWU, DU disposal at $11/kg of DU, and PWR fuel fabrication at $250/kg of LEU [156] to result in $1.123 M. Using this reference value, the unit price of various fuel fabrication activities, and variation in the required Nat-U, SWU, and DU tailings stream from Fig. 16, the cost of new fuel bundles, containing different mass and enrichment of LEU, is calculated.

References

[1] H.G. Rickover, The Decision to Use Zirconium in Nuclear Reactors, TID-26740, 1975.
[2] R.B. Adamson, in: G.P. Sabol, G.D. Moan (Eds.), Zirconium in the Nuclear Industry: 12th International Symposium, ASTM STP 1354, American Society for Testing and Materials, West Conshohocken, PA, 2000, p. 15.
[3] K. Edsinger, Nuclear News 53 (2010) 40.
[4] A. Strasser, J. Santucci, K. Lindquist, W. Yario, G. Stern, L. Goldstein, L. Joseph, An Evaluation of Stainless Steel Cladding for Use in Current Design LWRs, NP-2642. Electric Power Research Institute, Palo Alto, CA, 1982.
[5] B.A. Pint, K.A. Terrani, M.P. Brady, T. Cheng, J.R. Keiser, Journal of Nuclear Materials 440 (2013) 420–427.
[6] D. Dangouleme, V. Inozemtsev, K. Kamimura, J. Killeen, A. Kucuk, V. Novikov, V. Onufriev, M. Tayal, in: Proceedings of Top Fuel 2010, Orlando, FL, 2010.
[7] R.P. Knott, R.L. Kesterson, L.G. Hallstadius, M.Y. Young, in: Proceedings of Top Fuel 2003, Wurzburg, Germany, 2003.
[8] 10 Code of Federal Regulation 50.46.
[9] M. Billone, Y. Yan, T. Burtseva, R. Daum, Cladding Embrittlement During Postulated Loss-of-Coolant Accidents, NUREG/CR-6967. U.S. NRC, Office of Nuclear Regulatory Research, 2008.
[10] T. Cheng, J.R. Keiser, M.P. Brady, K.A. Terrani, B.A. Pint, Journal of Nuclear Materials 427 (2012) 396.
[11] R.E. Pawel, J.V. Cathcart, J.J. Campbell, Journal of Nuclear Materials 82 (1979) 129.
[12] J.-C. Brachet, L. Portier, T. Forgeron, J. Hivroz, D. Hamon, T. Guilbert, T. Bredel, P. Yvon, J.-P. Mardon, P. Jacques, in: G.D.M.a.P. Rudling (Ed.), Zirconium in the Nuclear Industry: Thirteenth International Symposium, ASTM STP 1423. ASTM International, West Conshohocken, PA, 2002, p. 673.
[13] C. Toffolon-Masclet, C. Desgranges, C. Corvalan-Moya, J.-C. Brachet, Solid State Phenomena 172–174 (2011) 652.
[14] M. Négyesi, J. Burda, O. Bláhová, S. Linhart, V. Vrtílková, Journal of Nuclear Materials 416 (2011) 288.
[15] J.-C. Brachet, V. Vandenberghe-Maillot, L. Portier, D. Gilbon, A. Lesbros, N. Waeckel, J.-P. Mardon, Journal of ASTM International 5 (2008).
[16] Draft Regulatory Guide DG-1263. U.S. Nuclear Regulatory Commission Office of Nuclear Regulatory Research, 2012.
[17] J. Alvis, W. Liu, R. Montgomery, Fuel Reliability Program: Proposed RIA Acceptance Criteria, Report No. 1021036. Electric Power Research Institute, Palo Alto, CA, 2010.
[18] Standard Review Plan for the Review of Safety Analysis Reports for Nuclear Power Plants, LWR Edition, NUREG-0800, Section 4.2 Fuel System Design, Rev. 3, U.S. Nuclear Regulatory Commission, Office of Nuclear Reactor, Regulation, March 2007.
[19] G. Wikmark, L. Hallstadius, K. Yueh, Nuclear Engineering and Technology 41 (2009) 143.
[20] P. Bossis, D. Pecheur, K. Hanifi, J. Thomazet, M. Blat, Journal of ASTM International 3 (2006) 494.
[21] G. Pan, C.J. Long, A.M. Garde, A.R. Atwood, J.P. Foster, R.J. Comstock, L. Hallstadius, D.L. Nuhfer, in: Proceedings of 2010 LWR Fuel Performance/TopFuel/WRFPM, Paper 74. American Nuclear Society, La Grange Park, Illinois, Orlando, Florida, 2010.
[22] Deterministic Safety Analysis for Nuclear Power Plants, Specific Safety Guide No. SSG-2. IAEA Safety Standards, 2009.
[23] N.E. Todreas, M.S. Kazimi, Nuclear Systems I: Thermal Hydraulic Fundamentals, Taylor and Francis, 1993.
[24] Fuel Cladding Failure Criteria, EUR 19256 EN. European Nuclear Commission, 1999.
[25] K.R. Robb, BWR Core Thermal Hydraulics under Short Term Station Blackout, ORNL, 2012.
[26] L. Baker, L.C. Just, Studies of Metal–Water Reactions at High Temperatures, ANL-6548, Argonne National Laboratory, 1962.
[27] M. Moalem, D.R. Olander, Journal of Nuclear Materials 182 (1991) 170.
[28] D.R. Olander, A.T. Motta, Light Water Reactor Materials (2012). in preparation.
[29] D.R. Olander, Nuclear Engineering and Design 148 (1994) 253.
[30] F. Fichot, B. Adroguer, A. Volchek, Y. Zvonarev, Nuclear Engineering and Design 232 (2004) 97.
[31] C. Corvalán-Moya, C. Desgranges, C. Toffolon-Masclet, C. Servant, J. Brachet, Journal of Nuclear Materials 400 (2010) 196.
[32] MELCOR, Developed at Sandia National Laboratories for the U.S. Nuclear Regulatory Commission. <http://melcor.sandia.gov>.
[33] Modular Accident Analysis Program (MAAP), developed by Fauske and Associates for the Electric Power Research Institute.
[34] L.J. Ott, K.R. Robb, D. Wang, J. Nucl. Mater. 448 (2014) 520–533.
[35] P. Hofmann, Journal of Nuclear Materials 270 (1999) 194.
[36] M. Steinbrück, M. Große, L. Sepold, J. Stuckert, Nuclear Engineering and Design 240 (2010) 1714.
[37] L. Ott, S. Hagen, Nuclear Engineering and Design 167 (1997) 287.
[38] R.S. Daum, S. Majumdar, Y. Liu, M.C. Billone, Journal of Nuclear Science and Technology 43 (2006) 1054.
[39] B.A. Pint, M.P. Brady, J.R. Keiser, T. Cheng, K.A. Terrani, in: Proceedings of the 8th International Symposium on High Temperature Corrosion and Protection of Materials, Les Embiez, France, 2012.
[40] K.A. Terrani, J.R. Keiser, M.P. Brady, T. Cheng, G.W. Silva, B.A. Pint, L.L. Snead, High Temperature Oxidation of Silicon Carbide and Advanced Iron-Based Alloys in Steam-Hydrogen Environments, TopFuel 2012, Manchester, UK, 2012.
[41] K.A. Terrani, C.M. Parish, D. Shin, B.A. Pint, Journal of Nuclear Materials 438 (2013) 64–71.
[42] J.V. Cathcart, R.E. Pawel, R.A. McKee, R.E. Druschel, G.J. Yurek, J.J. Campbell, S.H. Jury, Zirconium Metal–Water Oxidation Kinetics, IV: Reaction Rate Studies, ORNL/NUREG-17, Oak Ridge National Laboratory, 1977.
[43] V. Urbanic, T. Heidrick, Journal of Nuclear Materials 75 (1978) 251.
[44] S. Leistikow, G. Schanz, Nuclear Engineering and Design 103 (1987) 65.
[45] M. Steinbrück, N. Vér, M. Große, Oxidation of Metals 76 (2011) 215.
[46] H.C. Brassfield, J.F. White, L. Sjodahl, J.T. Bittel, Recommended Property and Reaction Kinetics Data for Use in Evaluating a Light–Water-Cooled Reactor Loss of Coolant Incident Involving Zircaloy-4 or 304SS Clad UO2, GEMP-482, General Electric Co., 1968.
[47] T. Ishida, Y. Harayama, S. Yaguchi, Journal of Nuclear Materials 140 (1986) 74.
[48] D. Young, D. Naumenko, L. Niewolak, E. Wessel, L. Singheiser, W. Quadakkers, Materials and Corrosion 61 (2010) 838.
[49] E.J. Opila, Trans Tech Publ (2004) 765.
[50] C. Tedmon, Journal of the Electrochemical Society 113 (1966) 766.
[51] D.J. Young, B.A. Pint, Oxidation of Metals 66 (2006) 137.
[52] R. Gauntt, D. Kalinich, J. Cardoni, J. Phillips, A. Goldmann, S. Pickering, M. Francis, K. Robb, L. Ott, D. Wang, C. Smith, S. St.Germain, D. Schwieder, C.

Phelan, Fukushima Daiichi Accident Study (Status as of April 2012), SAND2012-6173. Sandia National Laboratory, 2012.
[53] G.J. Walker et al., Transactions of American Nuclear Society (1970) 165.
[54] C. Cheng, Corrosion 20 (1964) 341.
[55] F. Garzarolli, R.V. Jan, H. Stehle, Atomic Energy Review 17 (1979) 31.
[56] S. Naymark, C. Spalaris, Proceedings: Nuclear fuels: 1. Fabrication and reprocessing. 2. Types and economics. 3. Raw materials 11 (1965) 425.
[57] L.L. Roddis, J.H. Ward, in, Proceeding of the 4th International Conference on the Peaceful Uses of Atomic Energy, A/CONF/49/P/036, Geneva, 1970.
[58] Oyster Creek Nuclear Power Plant Unit No.1, docket 50–129, Amendments 37, 40, 43, 1968.
[59] Review of Fuel Failures in Water Cooled Reactors, Report 1445. IAEA, Vienna, 2010.
[60] Fuel failure in normal operation of water reactors: Experience, mechanisms and management, IAEA TECDOC 709. IAEA, Vienna, 1993.
[61] R. Yang, B. Cheng, J. Deshon, K. Edsinger, O. Ozer, Journal of Nuclear Science and Technology 43 (2006) 951.
[62] Review of Fuel Failures in Water Cooled Reactors, IAEA Technical reports Series 388. IAEA, Vienna, 1998.
[63] V. Onufriev, IAEA Technical Working Group on Fuel Performance and Technology 24 (4) (2012).
[64] D.H. Locke, Nuclear Engineering and Design 33 (1975) 94.
[65] D.H. Locke, Nuclear Engineering International (1968).
[66] J.A. Pezzello, Transactions of American Nuclear Society (1975) 103.
[67] M.T. Simnad, Journal of Nuclear Materials 100 (1981) 93.
[68] G.S. Was, Y. Ashida, P.L. Andresen, Corrosion Reviews 29 (2011) 7.
[69] O.K. Chopra, A.S. Rao, Journal of Nuclear Materials 412 (2011) 195.
[70] O.K. Chopra, A.S. Rao, Journal of Nuclear Materials 409 (2011) 235.
[71] K. Ehrlich, J. Konys, L. Heikinheimo, Journal of Nuclear Materials 327 (2004) 140.
[72] S.J. Zinkle, J.T. Busby, Materials Today 12 (2009) 12.
[73] Y. Yamamoto, M.P. Brady, M.L. Santella, H. Bei, P.J. Maziasz, B.A. Pint, Metallurgical and Materials Transactions A 42A (2011) 922.
[74] R.L. Klueh, A.T. Nelson, Journal of Nuclear Materials 371 (2007) 37.
[75] D. Raabe, D. Ponge, O. Dmitrieva, B. Sander, Advanced Engineering Materials 11 (2009) 547.
[76] P.J. Ennis, in: K.B.S.R. B. Raj, T. Jayakumar, P.V. Sivaprasad, S. Saibaba, P. Shankar (Eds.), Advances in Stainless Steels, Universities Press, Hyderabad, India, 2010, p. 397.
[77] L. Tan, D.T. Hoelzer, J.T. Busby, M.A. Sokolov, R.L. Klueh, Journal of Nuclear Materials 422 (2012) 45.
[78] R.L. Cowan, in: R.H. Jones (Ed.), Chemistry and Electrochemistry of Corrosion and Stress Corrosion Cracking: A Symposium Honoring the Contributions of R.W. Staehle, The Minerals, Metals and Materials Society, Warrenton, PA, 2001, p. 467.
[79] R.W. Staehle, J.A. Gorman, in: 10th International Conference on Environmental Degradation of Materials in Nuclear Power Systems-Water Reactors. NACE, Lake Tahoe, CA, 2001, p. special bonus paper.
[80] D. Feron, J.-M. Olive, Corrosion Issues in Light Water Reactors–Stress Corrosion Cracking, CRC Press, Boca Raton, FL, 2007.
[81] S.S. Hwang, B.H. Lee, J.G. Kim, J. Jang, Journal of Nuclear Materials 372 (2008) 177.
[82] M. Le Calvar, I. De Curieres, in: D. Feron (Ed.), Nuclear Corrosion Science and Engineering, Woodhead Publishing Ltd., Oxford, 2012, p. 473.
[83] E.A. Kenik, J.T. Busby, Materials Science and Engineering R: Reports 73 (2012) 67.
[84] 10 Code of Federal Regulation 50 Appendix A.
[85] 10 Code of Federal Regulation 100.
[86] U.S. Nuclear Regulatory Commission, Regulatory Guide 1.70. Section 4.2.
[87] Schwarzkopf Plansee PM 2000, Sheet Grain Class 6 ODS Iron Alloy Sheet, material property datasheet, Material No.: 1.4768, Abbreviated DIN name: CrAl 21 6.
[88] Mechanical Properties INCOLOY alloy MA 956, material property datasheet.
[89] Kanthal APM and APMT Tube Material Datasheet, AB Sandvik Group, Sandviken, Sweden.
[90] High Temperature Characteristics of Stainless Steels, Report No. 9004. American Iron and Steel Institute, 2002.
[91] A.M. Garde, H.M. Chung, T.F. Kassner, Uniaxial Tensile Roperties of Zircaloy Containing Oxygen: Summary Report, ANL-77-30, Argonne National Lab, Argonne, IL, 1977.
[92] E.D. Hindle, D. Worswick, in: D.G. Franklin, R.B. Adamson (Eds.), Zirconium in the Nuclear Industry: Sixth International Symposium, ASTM STP 824, American Society for Testing and Materials, 1984, p. 133.
[93] S.-K. Kim, J.-G. Bang, D.-H. Kim, I.-S. Lim, Y.-S. Yang, K.-W. Song, D.-S. Kim, Nuclear Engineering and Design 239 (2009) 254.
[94] K.W. Lee, S.K. Kim, K.T. Kim, S.I. Hong, Journal of Nuclear Materials 295 (2001) 21.
[95] T. Onchi, H. Kayano, Y. Higashiguchi, Journal of Nuclear Materials 88 (1980) 226.
[96] K.J. Geelhood, C.E. Beyer, W.G. Luscher, Pacific Northwest National Laboratory (2008).
[97] C. Lemaignan, Comprehensive Nuclear Materials (2012) 217.
[98] H. Higgy, F. Hammad, Journal of Nuclear Materials 44 (1972) 215.
[99] F. Onimus, J.L. Béchade, Comprehensive Nuclear Materials (2012) 1.
[100] PLANSEE Metallwerk Plansee GmbH I Lechbruck, PM2000 Material Data Sheet, February 1993.
[101] Haddam Neck Plant – Decommissioning Updated Final Safety Analysis Report, CY-06-152. U.S. Nuclear Regulatory Commission, 2006.
[102] D. Powers, R. Meyer, Cladding Swelling and Rupture Models for LOCA Analysis, NUREG-0630, U.S. Nuclear Regulatory Commission, 1980.
[103] F. Erbacher, H. Neitzel, H. Rosinger, H. Schmidt, K. Wiehr, in: Zirconium in the Nuclear Industry: Fifth Conference, volume ASTM STP, 1982, p. 271.
[104] T. Forgeron, J. Brachet, F. Barcelo, A. Castaing, J. Hivroz, J. Mardon, C. Bernaudat, ASTM Special Technical Publication 1354 (2000) 256.
[105] F.J. Erbacher, S. Leistikow, A Review of Zircaloy Fuel Cladding Behavior in a Loss-of-Coolant Accident, Kernforschungszentrum Karlsruhe, 1985.
[106] K. Brickner, G. Ratz, R. Dumagala, ASTM STP 369 (1965) 99.
[107] M. Bocek, Journal of Nuclear Materials 82 (1979) 339.
[108] M. Mayuzumi, T. Onchi, Journal of Nuclear Materials 175 (1990) 135.
[109] R.L. Mehan, F.W. Wiesinger, Mechanical Properties of Zircaloy-2, KAPL-2110, Knolls Atomic Power Laboratory, Schenectady, NY, 1961.
[110] B. Clay, R. Stride, Nuclear Engineering and Design 48 (1978) 497.
[111] D.O. Northwood, I.M. London, L.E. Bahen, Journal of Nuclear Materials 55 (1975) 299.
[112] Z.L. Pan, N. Wang, Z. He, Measurements of Elastic Modulus In Zr Alloys For CANDU Applications, CW-128700-CONF-001, 11th International Conference on CANDU Fuel, Niagara Falls, Ontario, Canada, 2010.
[113] J.E. Pawel, A.F. Rowcliffe, G.E. Lucas, S.J. Zinkle, Journal of Nuclear Materials 239 (1996) 126.
[114] G.E. Lucas, Journal of Nuclear Materials 206 (1993) 287.
[115] P. Scott, Journal of Nuclear Materials 211 (1994) 101.
[116] S.M. Bruemmer, E.P. Simonen, P.M. Scott, P.L. Andresen, G.S. Was, J.L. Nelson, Journal of Nuclear Materials 274 (1999) 299.
[117] S.J. Zinkle, P.J. Maziasz, R.E. Stoller, Journal of Nuclear Materials 206 (1993) 266.
[118] S.I. Porollo, Y.V. Konobeev, A.M. Dvoriashin, A.N. Vorobjev, V.M. Krigan, F.A. Garner, Journal of Nuclear Materials 307–311 (2002) 339.
[119] R.L. Klueh, D.R. Harries, High-Chromium Ferritic and Martensitic Steels for Nuclear Applications, American Society for Testing and Materials, West Conshohocken, PA, 2001.
[120] T. Yamamoto, G.R. Odette, H. Kishimoto, J.-W. Rensman, P. Miao, Journal of Nuclear Materials 356 (2006) 27.
[121] M.A. Sokolov, H. Tanigawa, G.R. Odette, K. Shiba, R.L. Klueh, Journal of Nuclear Materials 367–370 (2007) 68.
[122] E. Gaganidze, H.C. Schneider, B. Dafferner, J. Aktaa, Journal of Nuclear Materials 367–370 (2007) 81.
[123] G.R. Odette, M.J. Alinger, B.D. Wirth, Annual Review of Materials Research 38 (2008) 471.
[124] D.A. McClintock, M.A. Sokolov, D.T. Hoelzer, R.K. Nanstad, Journal of Nuclear Materials 392 (2009) 353.
[125] H. Tanigawa, K. Shiba, A. Moslang, R.E. Stoller, R. Lindau, M.A. Sokolov, G.R. Odette, R.J. Kurtz, S. Jitsukawa, Journal of Nuclear Materials 417 (2011) 9.
[126] F.A. Garner, M.B. Toloczko, B.H. Sencer, Journal of Nuclear Materials 276 (2000) 123.
[127] J.-C. Brachet, X. Averty, P. Lamagnere, A. Alamo, F. Rozenblum, O. Raquet, J.-L. Bertin, Behavior of different austenitic stainless steels, conventional, reduced activation (RA) and ODS chromium-rich ferritic–martensitic steels under neutron irradiation at 325 deg C in PWR environment, Effects of Radiation on Materials: 20th International, Symposium, 2000, p. 500.
[128] M. Mathon, Y. De Carlan, G. Geoffroy, X. Averty, A. Alamo, C. De Novion, Journal of Nuclear Materials 312 (2003) 236.
[129] P. Grobner, Metallurgical and Materials Transactions B 4 (1973) 251.
[130] G. Bonny, D. Terentyev, L. Malerba, Journal of Phase Equilibria and Diffusion 31 (2010) 439.
[131] F. Danoix, P. Auger, Materials Characterization 44 (2000) 177.
[132] C. Capdevila, M.K. Miller, K.F. Russell, Journal of Materials Science 43 (2008) 3889.
[133] C. Capdevila, M.K. Miller, K.F. Russell, J. Chao, J.L. González-Carrasco, Materials Science and Engineering A 490 (2008) 277.
[134] E. Serra, G. Benamati, O. Ogorodnikova, Journal of Nuclear Materials 255 (1998) 105.
[135] C.S. Marchi, B. Somerday, S. Robinson, International Journal of Hydrogen Energy 32 (2007) 100.
[136] A. Garde, D. Mitchell, Comparison of Ductility of Irradiated ZIRLO and Zircaloy-4, Proceedings of TopFuel 2012, Manchester, United Kingdom, 2012.
[137] K. Ogata, T. Baba, K. Kamimura, J. Matsunaga, M. Nakatsuka, K. Sakamoto, A. Sawada, Effect of Increased Hydrogen Content on the Mechanical Performance of Irradiated Cladding tubes, Proceedings of TopFuel 2012, Manchester, United Kingdom, 2012.
[138] Y.R. Rashid, R.O. Montgomery, W.F. Lyon, Fracture Toughness Data for Zirconium Alloys: Application to Spent Fuel Cladding in Dry Storage, EPRI 1001281. Electric Power Research Institute, Palo Alto, CA, 2001.
[139] D. Gelles, Journal of Nuclear Materials 148 (1987) 136.
[140] R.A. Holt, Journal of Nuclear Materials 159 (1988) 310.
[141] T. Hirose, K. Shiba, M. Enoeda, M. Akiba, Journal of Nuclear Materials 367–370 (2007) 1185.

[142] K.H. Neeb, The radiochemistry of nuclear power plants with light water reactors, De Gruyter, 1997.
[143] L. Trevorrow, B. Kullen, R. Jarry, M. Steindler, Tritium and noble-gas fission products in the nuclear fuel cycle. I. Reactors, ANL-8102. Argonne National Lab., Ill. USA, 1974.
[144] W.E. Wang, D.R. Olander, Journal of the American Ceramic Society 78 (1995) 3323.
[145] J. Bell, J. Redman, H. Bittner, Journal of Materials for Energy Systems 1 (1979) 55.
[146] M.D. DeHart, S.M. Bowman, Nuclear Technology 174 (2011) 196.
[147] N.M. George, K.A. Terrani, J.J. Powers, Neutronic analysis of candidate accident tolerant fuel cladding concepts, ORNL/TM-2013/121, Oak Ridge National Laboratory, 2013.
[148] B. Cheng, Electric Power Research Institute, 2012.
[149] AP-1000 Design Control Document Rev. 16, Tier 2, Chapter 4, Section 4.1, ML071580895. U.S. Nuclear Regulatory Commission, 2007.
[150] Ventyx Velocity Suite, Energy Resources International, Inc., Nuclear Energy Institute, 2011. <http://www.NEI.org>.
[151] L.J. Siefken, E.W. Coryell, E.A. Harvego, J.K. Hohorst, SCDAP/RELAP5/MOD 3.3 Code Manual, NUREG/CR-6150, vol. 4, Rev. 2, 2001.
[152] I. Cohen, B. Lustman, J.D. Eichenberg, Journal of Nuclear Materials 3 (1961) 331.
[153] B.J. Ade, I.C. Gauld, Decay Heat Calculations for PWR and BWR Assemblies Fueled with Uranium and Plutonium Mixed Oxide Fuel Using Scale, ORNL/TM-2011/290, Oak Ridge National Laboratory, 2011.
[154] M.M. El-Wakil, Nuclear Heat Transport, American Nuclear Society, 1971.
[155] ANSI/ANS-5.1-2005: Decay Heat Power in Light Water Reactors American Nuclear Society, 2005.
[156] D.E. Shropshire, K.A. Williams, J.D. Smith, B.W. Dixon, M. Dunzik-Gougar, R.D. Adams, D. Gombert, J.T. Carter, E. Schneider, D. Hebditch, Advanced Fuel Cycle Cost Basis, INL/EXT-07-12107, Rev. 2. Idaho National Laboratory, 2009.
[157] K. Cohen, G.M. Murphy, The Theory of Isotope Separation as Applied to the Large-Scale Production of U235, McGraw-Hill, New York, 1951.